Experimental investigation of a multiphoton Heisenberg-limited interferometric scheme: The effect of imperfections

Shakib Daryanoosh ,* Geoff J. Pryde , Howard M. Wiseman ,† and Sergei Slussarenko ‡
Centre for Quantum Dynamics and Centre for Quantum Computation and Communication Technology, Griffith University, Yuggera Country, Brisbane, Queensland 4111, Australia

(Received 4 April 2024; revised 3 July 2024; accepted 3 July 2024; published 19 July 2024)

Interferometric phase estimation is an essential tool for precise measurements of quantities such as displacement, velocity, and material properties. The lower bound on measurement uncertainty achievable with classical resources is set by the shot-noise limit (SNL) that scales asymptotically as $1/\sqrt{N}$, where N is the number of resources used. The experiment of Daryanoosh *et al.* [Nat. Commun. **9**, 4606 (2018)] showed how to achieve the ultimate precision limit, the exact Heisenberg limit (HL), in *ab initio* phase estimation with $N = 3$ photon-passes, using an entangled biphoton state in combination with particular measurement techniques. The advantage of the HL over the SNL increases with the number of resources used. Here we present, and implement experimentally, a scheme for generation of the optimal $N = 7$ triphoton state. We study experimentally and theoretically the generated state quality and its potential for phase estimation. We show that the expected usefulness of the prepared triphoton state for HL phase estimation is significantly degraded by even quite small experimental imperfections, such as optical mode mismatch and unwanted higher-order multiphoton terms in the states produced in parametric downconversion.

DOI: 10.1103/PhysRevA.110.012614

I. INTRODUCTION

Phase measurement is an indispensable part of science and technology [1,2] as it offers simple yet robust methods for measuring a variety of physical quantities. Quantum mechanics bounds the ultimate precision in measurements to the Heisenberg limit (HL), which scales reciprocally with N (for large N), where N is the number of quantum resources. This contrasts with the shot noise limit (SNL), which is $1/\sqrt{N}$ asymptotically. Improving measurement precision beyond the SNL [3–5] towards the goal of achieving the best precision possible requires employing intrinsic quantum properties such as quantum superposition and entanglement in conjunction with other techniques.

Unlike phase sensing [6–11], which deals with the maximum sensitivity achievable in a measurement of a small variation of an already known parameter, *ab initio* phase estimation [12–16] aims at determining the exact value of the phase with no prior knowledge. In this situation, the exact optimal quantum precision, the exact HL, is π/N in the asymptotic regime [17].

This exact optimal precision can be achieved by an interferometric Heisenberg-limited phase estimation algorithm [18] (HPEA), as has since been demonstrated experimentally with photonic qubits [16]. That experiment relied on three techniques to attain uncertainty very close to the exact HL for $N = 3$ resources: the use of the optimal entangled two-qubit state preparation, multiple application of the phase shift, and performing adaptive measurements [18]. Here, as is standard in quantum metrology [3,19], a single resource corresponds to a single qubit passing through a rotation by the unknown phase.[1] For the case $N = 3$, one photonic qubit passes the phase shift once and the other twice.

Two-photon probe states are relatively easy to generate with spontaneous parametric downconversion (SPDC) photon sources and small-scale optical circuits. But to obtain a greater quantum advantage over classical measurement schemes, per resource used, larger multiphoton probe states and thus more complex optical state generation schemes are needed.

In this work, we study both theoretically and experimentally the $N = 7$ version of HPEA in the presence of experimental imperfections. We theoretically investigate the protocol under the influence of optical mode mismatch and noise coming from the unwanted photon emission events from the photon sources. We analyze these effects separately due to the computational complexity of simulations. Our results indicate that the quality of phase estimation is highly sensitive to these imperfections. Next we implement experimentally a setup for generating the optimal [18] three-qubit ($N = 7$ resources) probe state. This is an unusual three-photon state that

*Contact author: shakib.daryanoosh@uwa.edu.au
†Contact author: h.wiseman@griffith.edu.au
‡Contact author: s.slussarenko@griffith.edu.au

[1] In the traditional way of resource counting, only the number of probes are taken into account. If one were to follow this method, then phase estimation uncertainty violates the HL scaling. Ignoring the number of passes can lead to arbitrarily small phase uncertainty. For instance, via nondemolition measurements of a single photon, an interferometric phase estimation scheme can be repeated as many times as desired to attain exponentially small phase sensitivity [18].

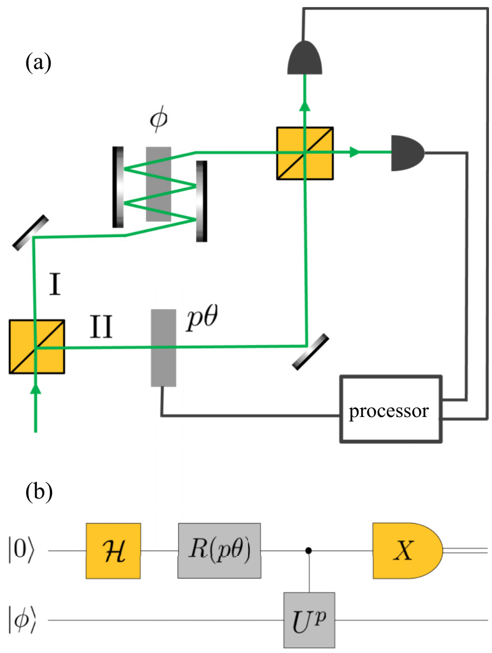

FIG. 1. (a) Schematic representation of the modified Mach-Zehnder interferometer allowing for multiple applications of the phase element ϕ. The optical mode in path "I" passes multiple (p) times (here $p = 4$) such that a total phase shift of $p\phi$ is acquired. Also the reference phase in path "II" is set so that it imparts θ phase shift. (b) Quantum circuit illustration for the interferometric phase estimation scheme with one qubit using the interferometer from (a).

has not been reported in prior experimental literature. Feeding the tomographically reconstructed experimental probe state into a stochastic simulation of the phase estimation protocol, we find out that its quality is insufficient for measuring phase with precision near the HL. In fact, the phase uncertainty is greater than the SNL because of experimental challenges such as maintaining the setup stability over the course of experiment.

The paper is outlined as follows: In Sec. II we overview the Heisenberg-limited phase estimation algorithm and design a quantum circuit for creating the optimal state using three photonic polarization qubits. Section III deals with modeling optical mode mismatch and multiphoton pair generation in the SPDC process, respectively. Experimental results are discussed in Sec. IV, followed by a conclusion in Sec. V.

II. THEORY

A. Interferometric phase estimation

HPEA can be executed on a modified Mach-Zehnder interferometer (MZI) depicted in Fig. 1(a). The unknown phase ϕ is placed in arm "I" of the interferometer. The arm is configured in such a way that it allows an optical mode to pass through a phase shift element p times so that the total phase of $p\phi$ would be acquired by a single photon. The other arm ("II") of the interferometer contains a reference phase θ. This phase can be adjusted over the course of the experiment [20,21]. That is, after each detection, the measurement outcomes are analyzed in a processor unit, and based on the results, θ is adjusted according to the protocol in Ref. [22].

In the context of quantum information, an interferometric phase measurement scheme can be mapped onto a quantum circuit. This becomes handy when it comes to considering various phase estimation algorithms. The two arms of the interferometer correspond to the two basis states $|0\rangle$ and $|1\rangle$ of a qubit. An input qubit is then represented by the logical state $|0\rangle$. A beam splitter (BS) that the photon impinges on performs a Hadamard operation $\mathcal{H}|0\rangle(|1\rangle) = |+\rangle(|-\rangle)$, where $|\pm\rangle \equiv (|0\rangle \pm |1\rangle)/\sqrt{2}$. The unknown phase shift $p\phi$ is represented by the controlled unitary (CU) operator $|1\rangle\langle 1| \otimes \hat{U}^p + |0\rangle\langle 0| \otimes \hat{I}$, where $\hat{U}|\phi\rangle = e^{i\phi}|\phi\rangle$ acts on an additional register in state $|\phi\rangle$, and $\hat{I}$ is the identity operator. The auxiliary phase shift θ is represented by $\hat{R}(\theta) \equiv \exp(i\theta|0\rangle\langle 0|)$. The system state after the second BS undergoes a basis transformation $Z \to X$, that is, from the logical to the $|\pm\rangle$ basis. This implies that the latter BS can be replaced with a measurement stage in the X basis. Therefore, estimating the phase using this interferometric algorithm is described by the quantum circuit illustrated in Fig. 1(b).

Utilizing path-entangled NOON states or multipassing can improve the sensitivity in a phase measurement compared to a repeated single-photon single-pass measurement [18]. At the same time, they reduce the range of phase value that can be distinguished, making it impossible to distinguish phase values that differ by more than π/p. To perform an *ab initio* phase estimation, one needs to remove this ambiguity in phase measurement and extend the range of the measurement to the full $[0, 2\pi)$ interval. This can be achieved with an appropriate choice of the probe state and measurement protocol.

To evaluate the performance of phase measurement protocols, we use the Holevo measure of deviation defined as [23]

$$D_{\mathrm{H}} = |\langle\langle \exp[i(\phi - \phi_{\mathrm{est}}(y))]\rangle_y\rangle_\phi|^{-2} - 1. \tag{1}$$

Here y is the data from which the estimate is made, and $\langle\cdots\rangle_\bullet$ represents the ensemble average of the expression inside the angled brackets over $\bullet$. This measure is minimized for the optimal estimate,

$$\phi_{\mathrm{est}}(y) = \arg\langle\exp(i\phi)\rangle_{\phi|y}, \tag{2}$$

where $\langle\cdots\rangle_{\bullet|y}$ means that there the average is conditioned (in a Bayesian way) on the data y. For this choice, which we will make henceforth, the Holevo deviation is equal to what has been dubbed the Holevo variance,

$$V_{\mathrm{H}} = \left(\langle|\langle\exp(i\phi)\rangle_{\phi|y}|\rangle_y\right)^{-2} - 1. \tag{3}$$

This metric respects the cyclic property of the phase and sets the upper bound on the precision scaling in a sense that any other variance-like measure will scale at least as well as Holevo variance, whereas the reverse is not necessarily true [21].

B. Quantum phase estimation algorithm

The HPEA is built upon the quantum phase estimation algorithm (QPEA) of Cleve *et al.* [24]; see Fig. 2. At the core of QPEA lies an inverse quantum Fourier transformation (IQFT) that can be implemented with a scheme based on single-qubit

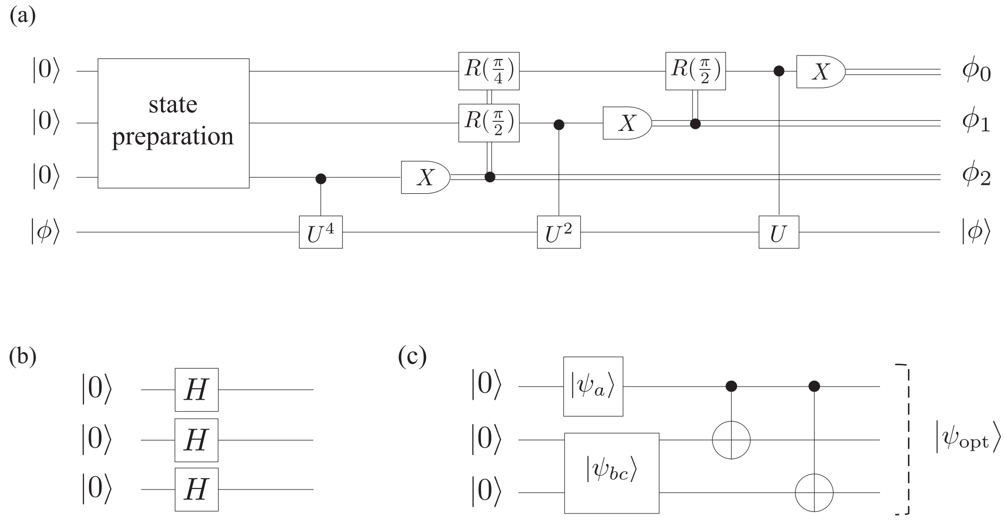

FIG. 2. (a) Circuit diagram for the Heisenberg-limited interferometric phase estimation binary encoding for probe qubits with $N = 7$ quantum resources. (b) State preparation for the QPEA: a Hadamard operation is applied on each qubit in the same way as depicted in Fig. 1. (c) Circuit representation for creating the three-photon optimal state, Eq. (10). The input state, $|\psi_{\rm in}\rangle = |\psi_a\rangle|\psi_{bc}\rangle$, is transformed into the optimal state, after application of two consecutive CNOT gates.

inputs, single-qubit measurements, and classical feed-forward on the reference phase θ [25]. The Holevo variance of the QPEA scales theoretically as [26]

$$V_{\rm H}^{\rm QPEA} = \frac{2}{N} + \frac{1}{N^2}, \tag{4}$$

which is above the SNL even for large N. The failure of the QPEA in this task can be understood by examining the probability distribution function $P(\phi_{\rm est})$ for the phase estimate, given by [26]

$$P(\phi_{\rm est}) = \frac{1}{2\pi}\left|\sum_{n=0}^{N} \mathcal{C}_n e^{-in(\phi_{\rm est}-\phi)}\right|^2, \tag{5}$$

where $\mathcal{C}_n = \frac{1}{\sqrt{N+1}}$. This distribution profile [shown in Fig. 3(a) for the case of $N = 3$ and 7] shows a sharp peak around $\phi_{\rm est} = \phi$, with width scaling as $1/N$ (as desired), but with relatively high wings. The envelope of the distribution for the wings falls off as the inverse square of the error in the estimate $(\phi_{\rm est} - \phi)^{-2}$, which gives rise to the leading order term in Eq. (4). Although QPEA can be improved by using a more complex adaptive measurement scheme [12,19], even the generalized QPEA can only achieve Heisenberg scaling in precision (with a constant overhead), but not the exact HL.

C. Heisenberg-limited optical phase estimation scheme

The key difference that allows HPEA to theoretically achieve the exact HL precision is the use of the optimal entangled probe state as the input to the QPEA. The quantum circuit for both the QPEA and HPEA for $N = 7$ resources is shown in Fig. 2(a). For the general case of $N = 2^{K+1} - 1$, a register of $K + 1 = 3$ qubits is prepared in a product state for the QPEA, Fig. 2(b), and in a particular entangled state for the HPEA, Fig. 2(c). Then, 2^k CU gates are applied sequentially to each qubit followed by the measurement in the X basis, starting from the qubit labeled by $k = K$. The result of the measurement classically controls reference rotation operations on the remaining qubits. The protocol proceeds downwards in k until the qubit labeled by $k = 0$ is measured. The kth measurement yields the kth bit in the binary expansion bit of $\phi/2\pi$. That is, the phase estimate is obtained according to the following

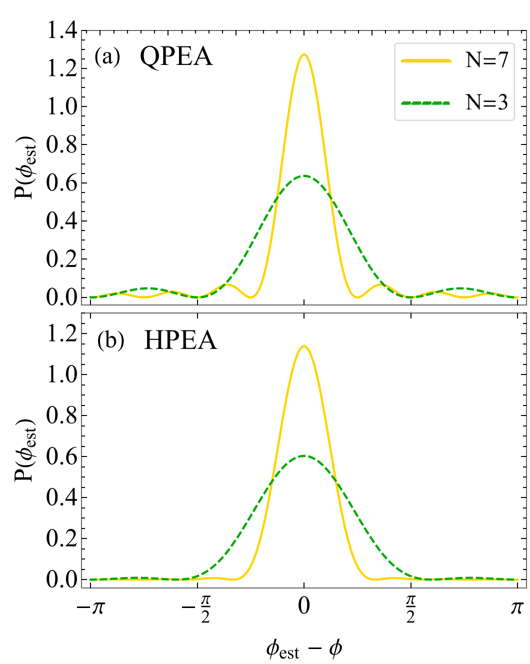

FIG. 3. Probability distribution function for (a) the QPEA and (b) the HPEA for two different numbers of quantum resources $N = 3$ (dashed green) and $N = 7$ (solid gold). It can be clearly seen that employing more resources results in a localized distribution function around $\phi_{\rm est} = \phi$. Optimizing the input state to the QPEA, the impact of rather high tails on phase estimation can be alleviated.

relation:

$$\phi_{\text{est}} = 2\pi \times 0.\phi_0\phi_1 \cdots \phi_K = 2\pi \sum_{k=0}^{K} \frac{\phi_k}{2^{(k+1)}}. \tag{6}$$

For canonical (optimal) measurements, the optimal state takes the following form [27]:

$$|\Psi_{\text{opt}}\rangle \propto \sum_{n=0}^{N} \psi_n |n\rangle, \tag{7}$$

where

$$\psi_n = \sin\left[\frac{(n+1)\pi}{N+2}\right], \tag{8}$$

$|m\rangle$ is the logical state of a register of qubits, and m is a binary digit string of length $K+1$. The probability distribution function for estimating phase using this optimal state can be written in the same form as in Eq. (5) but with $\mathcal{C}_n = \psi_n / \sum_{n=0}^{N} |\psi_n|^2$. Note that the latter coefficients are in marked contrast to those of the QPEA, which are independent of n.

The effect of input state optimization is to improve the phase estimation by reducing the high tails present in $P(\phi_{\text{est}})$ for the QPEA. Figure 3(b) illustrates this feature by plotting the probability distribution function for the phase estimate employing the optimal state, Eq. (7).

Using this state, the Holevo phase variance, Eq. (3), is minimized. That is, the interferometer attains its ultimate precision, the exact HL, which is expressed as [27]

$$V^{\text{HL}} = \tan^2\left(\frac{\pi}{N+2}\right). \tag{9}$$

D. Creating the optimal three-photon state

For the $N = 7$ case, using the polarization degree of freedom to encode the qubits (i.e., horizontal $|H\rangle \equiv |0\rangle$, vertical $|V\rangle \equiv |1\rangle$), the normalized optimal state Eq. (7) can be written as

$$|\psi_{\text{opt}}\rangle = \sum_{j=0}^{3} \alpha_j |\text{GHZ}_j\rangle, \tag{10}$$

where $|\text{GHZ}_j\rangle$ are Greenberger-Horne-Zeilinger type states [28],

$$|\text{GHZ}_0\rangle = (|HHH\rangle + |VVV\rangle)/\sqrt{2}, \tag{11a}$$

$$|\text{GHZ}_1\rangle = (|HHV\rangle + |VVH\rangle)/\sqrt{2}, \tag{11b}$$

$$|\text{GHZ}_2\rangle = (|HVH\rangle + |VHV\rangle)/\sqrt{2}, \tag{11c}$$

$$|\text{GHZ}_3\rangle = (|HVV\rangle + |VHH\rangle)/\sqrt{2}, \tag{11d}$$

and

$$\alpha_j = \sqrt{2/\mathcal{N}} \sin[(j+1)\pi/9], \tag{12a}$$

$$\mathcal{N} = 2\sum_{j=0}^{3} \sin^2[(j+1)\pi/9]. \tag{12b}$$

Here $|HHH\rangle$ denotes $|H_a\rangle \otimes |H_b\rangle \otimes |H_c\rangle$, and the labels "$a$," "$b$," and "$c$" correspond to the input qubits $k = 0$, 1, and 2, respectively. The optimal state can be realized with the circuit depicted in Fig. 2(c), in which two CNOT gates are sequentially applied to the input state $|\psi_{\text{in}}\rangle = |\psi_a\rangle|\psi_{bc}\rangle$, where $|\psi_a\rangle = |+\rangle$ and

$$|\psi_{bc}\rangle = \alpha_0|HH\rangle + \alpha_1|HV\rangle + \alpha_2|VH\rangle + \alpha_3|VV\rangle, \tag{13}$$

with α_i satisfying Eqs. (12a)–(12b). Using $\hat{U}_{\text{CT}}^{\text{CNOT}}$ for the CNOT operation between the control (C) and target (T) qubit, the output state can be written

$$|\psi_{\text{out}}\rangle = \hat{U}_{ac}^{\text{CNOT}}\, \hat{U}_{ab}^{\text{CNOT}}\, |\psi_{\text{in}}\rangle \equiv |\psi_{\text{opt}}\rangle. \tag{14}$$

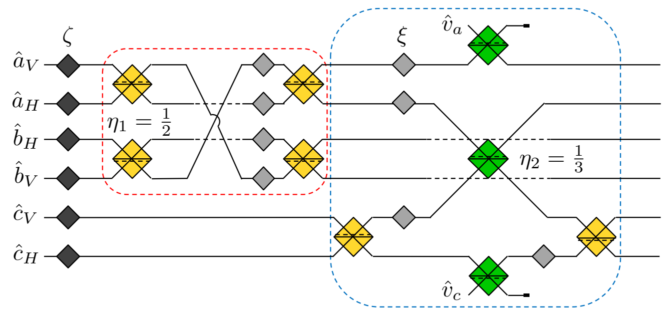

FIG. 4. Conceptual circuit diagram for creating the optimal three-photon state, Eq. (10), consisting of two probabilistic CNOT gates. The dashed-red panel indicates a nonuniversal CNOT (NCN) gate operating between qubits labeled "a" and "b," where each is modeled by two polarization modes H and V. The gold diamonds are beam splitters with reflectivity coefficient $\eta_1 = \frac{1}{2}$; the dashed lines inside the beam splitters show that a photon reflected off that side acquires π phase shift. Upon successful coincidence detection of photons, this gates produces the state $|\psi_1\rangle$, Eq. (15), with probability $\wp_{\text{NCN}} = \frac{1}{2}$. The dashed-blue panel indicates a universal CNOT (CN) gate acting between qubits labeled "a" and "c." Each of these qubits has a vacuum port with an appropriate annihilation operator $\hat{v}_a$ and $\hat{v}_c$, respectively. The green diamonds are beam splitters with reflectivity $\eta_2 = \frac{1}{3}$. The gate successfully operates with probability $\wp_{\text{CN}} = \frac{1}{9}$ due to postselection. The black and gray diamonds illustrate beam splitters with reflectivity ζ and ξ, respectively, for modeling total inefficiency in detecting photons and mode mismatch, respectively. Each of these BSs is treated in the same way explained in Sec. III.

A concrete optical circuit to realize the state generation scheme is depicted in Fig. 4. Here $\hat{a}_V \cdots \hat{c}_H$ are the annihilation operators of the corresponding orthogonal polarization modes of photons "a," "b," and "c," respectively, and we use dual-rail encoding [29], meaning that a single-photon occupation of one of the orthogonal modes of the same photon corresponds to a logical $|0\rangle$ or $|1\rangle$ state.

We use two types of probabilistic CNOT gates in our circuit. The $\hat{U}_{ab}^{\text{CNOT}}$ operation is realized with a probabilistic nonuniversal CNOT (NCN) gate Ref. [30]. Here "nonuniversality" means that it does not operate as a CNOT gate for a general two-qubit state but for a subset of bipartite state space. This gate is schematically shown in Fig. 4 inside the dashed-red box including four beam splitters with reflectivity $\eta_1 = \frac{1}{2}$ operating between the photons in modes "a" and "b." We note that the black and gray diamonds should be ignored throughout this section as they account for modeling imperfections, which will be dealt with in Sec. III.

The task of the NCN is to entangle photons a and b by creating the state

$$|\psi_1\rangle = \left(\hat{U}_{ab}^{\mathrm{CNOT}} \otimes \hat{I}_c\right)|\psi_{\mathrm{in}}\rangle, \tag{15}$$

which is the first part of $|\psi_{\mathrm{out}}\rangle$ in Eq. (14). Here $\hat{I}_c$ denotes an identity operation on the mode labeled "c." With the input in modes "b" and "c" as Eq. (13) and $|\psi_a\rangle = |H\rangle$, the output of the NCN is

$$\left|\psi_{\mathrm{out}}^{\mathrm{NCN}}\right\rangle = \frac{1}{\sqrt{2}}(|\psi_1\rangle + |\psi_d\rangle), \tag{16}$$

where $|\psi_d\rangle$ represents a superposition of states with more than one photon in either of modes[2] and it can be filtered out with an appropriate coincidence measurement. The result in Eq. (16) shows that the state $|\psi_1\rangle$ is nondeterministically generated upon postselection with probability success $\wp_{\mathrm{NCN}} = \frac{1}{2}$.

The dashed-blue box in Fig. 4 shows a probabilistic universal CNOT (CN) gate [31] between the two modes of the photon "c" (the target qubit) and the photon labeled "a" (the control qubit). Photons in modes a_H and c_V nonclassically interfere on the central (green) BS with reflectivity $\eta_2 = \frac{1}{3}$. There are two other such BSs, one of them located on the lower arm of the interferometer with the vacuum mode v_c and the other one affecting only the control photon with the vacuum mode v_a. It was demonstrated in Refs. [32,33] that for a general two-photon state such as Eq. (13) this CNOT gate works with a probability of success $\wp_{\mathrm{CN}} = \frac{1}{9}$. By using the combination of NCN and CN, the optimal state is nondeterministically obtained with the probability of success $\wp_{\mathrm{opt}} = \frac{1}{18}$. The postselected successful operations correspond to the cases when each of the three outputs in Fig. 2(c) contains at least one photon. Comparing to the circuit that uses two CN gates with an overall probability of success of $\frac{1}{81}$, the advantage of using a NCN-NC circuit becomes clear. The detailed procedure for the calculation of the optimal state generation circuit is described in Appendix A.

E. Analysis of the HPEA

At the end of the phase measurement protocol, each projective measurement yields one of the binary bits ϕ_k required for estimating the phase. The probability of getting a string $\phi_0\phi_1\cdots\phi_K$ of binary digits pattern, corresponding to one of the 2^{K+1} possible outcomes, is asymptotically ($n_{\mathrm{ens}} \to \infty$) equal to the number of times $n_{\phi_0\phi_1\cdots\phi_K}$ that measurement result turns up divided by the size n_{ens} of the ensemble over which the Holevo deviation calculations are done:

$$P_{\phi_0\phi_1\cdots\phi_K} = \frac{n_{\phi_0\phi_1\cdots\phi_K}}{n_{\mathrm{ens}}}. \tag{17}$$

To calculate the Holevo deviation, a few more steps should be carried out. First, the ensemble average of $e^{i[\phi-\phi_{\mathrm{est}}(y)]}$ over the measurement results $y \in \{\phi_0\phi_1\phi_2\}$ needs to be worked out for calculating the deviation according to Eq. (1). That is, by choosing a phase in the interval $[0, 2\pi)$, and setting $\phi_{\mathrm{est}}(y)$ according to Eq. (6), one obtains the phase-dependent deviation[3]

$$D_{\mathrm{H}}^{\phi} = |\langle \exp[i(\phi - \phi_{\mathrm{est}}(y))]\rangle_y|^{-2} - 1. \tag{18}$$

Then, by erasing this initial phase information in the way defined in Eq. (1), the phase-independent Holevo deviation D_{H} is determined. Figure 5 demonstrates simulation results for the optimal protocol using the state $\hat{\rho}_{\mathrm{opt}}$ given in Eq. (10) for both of these quantities in orange dots and the purple horizontal line-segment cutting the left axis, respectively. The latter, up to an infinitesimal numerical error, is equal to the Heisenberg limit $V^{\mathrm{HL}} = 0.132\,474\ldots$ obtained by letting $N = 7$ in Eq. (9). The procedure for stochastic simulations of the measurement circuit is described in Appendix B.

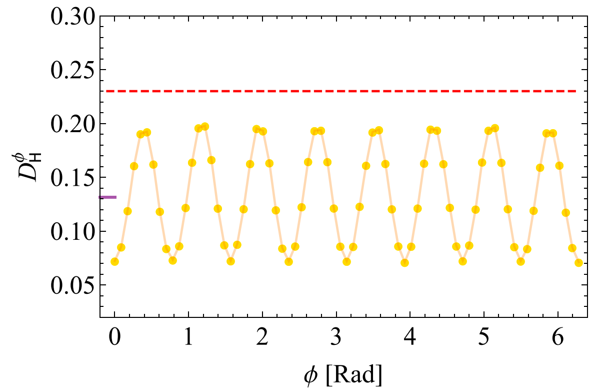

FIG. 5. Variation of the phase-dependent deviation, Eq. (18), as a function of phase for the optimal three-photon state ρ_{opt}, for the $K = 2$ ($N = 7$) HPEA (circular orange). For *ab initio* phase estimation, the Holevo deviation, Eq. (1), is used, an average that corresponds to erasing any prior information about the phase. For measurements performed on the ideal state, this is depicted by a purple horizontal line. The *ab initio* SNL is shown by a dashed red line. Note that since the probe state assumed here is perfect, the estimate from the HPEA would be optimal, Eq. (2), so the Holevo deviation is equal to the Holevo variance, Eq. (3).

The shot-noise limit $V_{\mathrm{SNL}} = 0.232\,688\ldots$ is depicted by the dashed-red line. In the SNL-limited measurement, uncorrelated photons are sent through the unknown phase and each is measured at its own measurement angle. To calculate the true SNL, we minimize the variance as a function of these measurement angles. It is worth noting that if such a minimization procedure is applied for the $N = 3$ measurement, the corresponding SNL bound is $V_{\mathrm{SNL}} = 0.655\,845\ldots$ instead of $V_{\mathrm{SNL}} = 0.777\,777\ldots$, reported in Ref. [16], where the three photons were measured at different equidistant angles in $[0, 2\pi)$. See Appendix C for details on the calculations and measurement angles.

As can be seen, the profile of D_{H}^{ϕ} shows peaks and troughs around the HL with minima occurring at multiples of $\pi/4$. Each minimum equals one of the eight estimated phases ϕ_{est} that are possible from the eight possible results $\phi_0\phi_1\phi_2$. This

[2]This depends on the value of the complex amplitudes α_j in Eq. (13). For example, the mode labeled $\hat{a}_V$ can be in a two-photon state with probability $\frac{1}{16}(|\alpha_2 - \alpha_0|^2 + |\alpha_3 - \alpha_1|^2)$.

[3]Note that for the reconstructed state tomography, $\phi_{\mathrm{est}}(y)$ is set slightly different from this ideal scenario, which will be explained in Sec. IV.

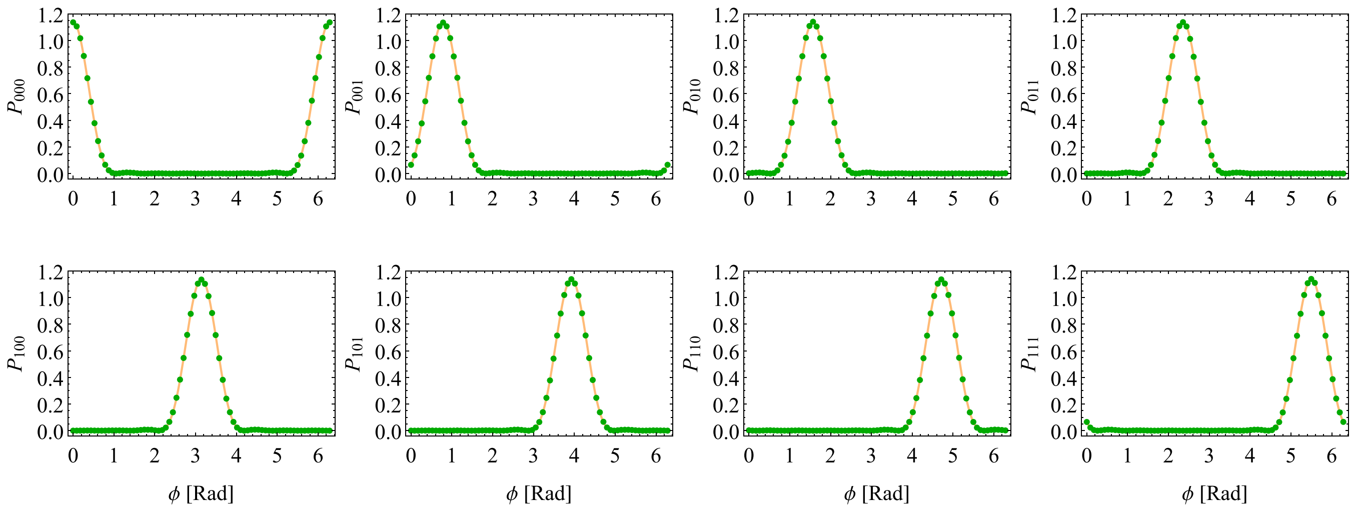

FIG. 6. (Normalized) probability distribution, Eq. (17), of different measurement results as a function of phase for the HPEA for $K = 2$ ($N = 7$). It is expected that when the true phase, ϕ, is equal to one of the eight possible binary digits sequences, $(\phi_0\phi_1\phi_2) \in \{000, 001, \ldots, 111\}$, the phase estimation algorithm's precision is at its best. The green dots are the results of numerical simulations, and the solid gold curves are obtained via Eq. (5) with the corresponding $\mathcal{C}_n$ for the HPEA. In all plots, $n_{\text{ens}} = 50 \times 10^3$.

is also understood by analyzing the probability distribution for the above measurement output set; see Fig. 6. For those phases for which $D_{\rm H}^{\phi}$ is minimum, the corresponding probability density function is maximum. In contrast, for points in between minima, the phase-dependent deviation shows a less accurate estimation of the phase. Nevertheless, since we are interested in *ab initio* phase measurement, the knowledge about phase can be removed by averaging over ϕ to obtain a precision value applicable to the entire range of $[0, 2\pi)$.

The oscillatory behavior of $D_{\rm H}^{\phi}$ shown in Fig. 5 depends on the number of resources employed. The higher N means oscillations with a larger frequency and smaller amplitude. For example, comparing the scenario here ($N = 7$) with the two-photon $N = 3$ resources studied in Ref. [16], the number $N + 1 = 2^{K+1}$ of oscillations doubled and the amplitude decreased by an order of magnitude.

III. THE EFFECT OF IMPERFECTIONS

So far in our analysis of the Heisenberg-limited phase estimation algorithm, everything took place in an ideal world. However, one should take into account practical considerations when it comes to realizing such protocols in laboratories. This is typical in almost all physical experiments, and in particular, it is one of the important challenges in quantum metrology [34–37]. Quantum-enhanced phase estimation schemes suffer from experimental imperfection in state preparation and detection. In quantum optics, these may be associated with optical mode mismatch (which leads to degraded nonclassical interference), the presence of multiphoton emission noise in imperfect single-photon sources, inefficient detectors, and the lack of photon-number resolving detectors. In what follows, we first present a model to address optical mode mismatch and imperfect detection, and then separately consider the effect of multiphoton generation events on state preparation.

A. Optical mode mismatch

Central to the probabilistic CNOT gates considered in the previous section is the non-classical Hong-Ou-Mandel (HOM) interference phenomenon [38]. Two photons incident on a beam splitter perfectly interfere only if they cannot be distinguished from each other. This requires both of them to be in the same spatial, temporal, spectral, and polarization modes. Any partial distinguishability of photons results in imperfect interference of quantum fields, which ultimately limits an experimenter's ability to prepare the desired optimized state.

One way to model mode mismatch in HOM interference on a beam splitter is illustrated in Fig. 7. This model is employed in the state preparation shown in the circuit diagram, Fig. 4. The two extra vacuum modes v_a and v_b are introduced for the main part of the incoming beams in modes a and b, respectively. In addition, two other auxiliary vacuum modes v_1 and v_2 are included in the model for overlapping with v_a and v_b, respectively. We characterize the degree to which the modes overlap by the BSs reflectivities ξ_j ($j = 1, 2$) prior to

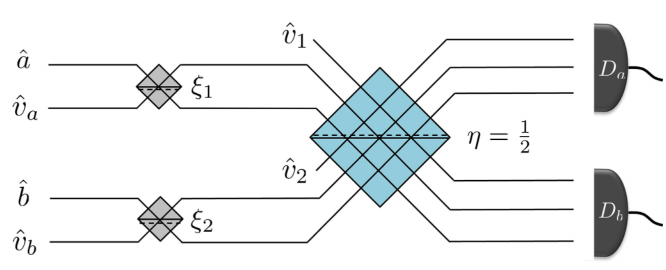

FIG. 7. Conceptual diagram of Hong-Ou-Mandel interferometer for modeling spatial optical mode matching. The imperfect overlap of modes is modeled by splitting the input beams (modes $\hat{a}$ and $\hat{b}$), via the gray BSs with reflectivities ξ_j, into two modes each such that only some portion of them interfere. $\hat{v}_j$ represent vacuum mode annihilation operators. In this case, we show a 50:50 beamsplitter.

the interference beam splitter. The ideal case obviously takes place when $\xi_j = 1$, for which the two modes perfectly overlap. This scheme is easiest understood in terms of spatial mode overlap, but it is also applicable to modeling mismatch in any other single degree of freedom.

To see how any mode mismatch leads to deteriorated quantum interference, we calculate the probability $\wp_{\text{coin}}$ of measuring a coincidence photon detection at detectors D_a and D_b,

$$\wp_{\text{coin}} = \langle \hat{n}_{D_a} \hat{n}_{D_b} \rangle = \tfrac{1}{2}(1 - \xi_1 \xi_2), \tag{19}$$

where $\hat{n}_{D_a}$ and $\hat{n}_{D_b}$ are the photon number operators for the bundle of three modes detected in each detector. The above expectation value is calculated using the input state $|\mathbb{0}\rangle_{\hat{v}_1} \otimes |\mathbb{0}\rangle_{\hat{v}_2} \otimes |\mathbb{0}\rangle_{\hat{v}_3} \otimes |\mathbb{0}\rangle_{\hat{v}_4} \otimes |\mathbb{1}\rangle_{\hat{a}} \otimes |\mathbb{1}\rangle_{\hat{b}}$. Here $|\mathbb{0}\rangle$ and $|\mathbb{1}\rangle$ denote the vacuum and single-photon state, respectively. That is, the two modes indicated by $\hat{a}$ and $\hat{b}$ are in a single-photon state, and the rest are in the vacuum state. Ideally, a coincidence detection happens between modes a and b, whereas for the scenario sketched here, nine coincidence detection possibilities occur. The algebra leading to Eq. (19) is straightforward and can be found in Appendix D. Note that for the perfect mode matching $\xi_1 = \xi_2 = 1$ the coincidence probability is zero, as expected in an ideal HOM interference phenomenon. This probability also acquires its classical value of $\wp_{\max} = \frac{1}{2}$ for the case of no overlap of the modes when either of the BSs is totally transmitting, $\xi_j = 0$.

A good measure that can capture the effect of mode mismatch is the quality of interference fringes or nonclassical interference of photons known as dip visibility,

$$\nu = [\wp_{\max} - \wp_{\text{coin}}]/\wp_{\max} = \xi_1 \xi_2. \tag{20}$$

From this relation it can be easily seen that for an ideal overlapping of modes where both auxiliary BSs are totally reflecting, the visibility is 1 and it becomes 0 for $\xi_j = 0$, where the two modes completely mismatch. The worse the mode matching, the greater the deviation of dip visibility from its ideal value of 1.

Now this model can be incorporated into the mode calculation analysis for the optimal state preparation. An implication of this is that the generated state will no longer be the same as ρ_{opt} and as a consequence the protocol's performance in estimating phase drops. To see this effect, we place some beam splitters with reflectivity ξ at relevant beam paths, shown by gray diamonds in Fig. 4. This means some auxiliary modes are introduced in the same way as discussed above. Note that the inserted BSs do not have to be identical. Nevertheless, assuming alike BSs is a good approximation of a real experimental scenario. Another type of auxiliary BSs with reflectance coefficient ζ, illustrated in Fig. 4 as black diamonds, is used to model non-unit-efficiency of the photon detectors. One can introduce these latter BSs in the very beginning of the circuit due to the linearity of optical elements, which allows us to shift them through all the way from the detection stage.

Incorporating all these auxiliary beam splitters and modes into the state preparation circuit allows for conducting numerical simulations[4] to determine the Holevo deviation for different amounts of mode mismatch. This is depicted in Fig. 8, where the dashed green line shows the SNL, and golden data points are the results of numerical simulations. Supposing there are no other experimental imperfections, the sub-shot-noise precision would not be observed for mode mismatch above about 7%. In an ideal condition $\xi = 1$, the protocol performs at the exact Heisenberg limit, as expected.

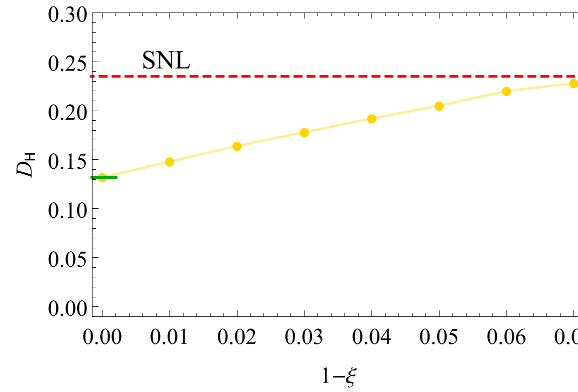

FIG. 8. Impact of optical mode mismatch on the overall performance of the HPEA. The result of numerical simulations of the Holevo deviation, Eq. (1), is illustrated using golden solid points (the solid golden line is a guide for the eyes). The green dashed line depicts the SNL. Heralding efficiency is set at 13% for all simulations, and each point is obtained using 10^4 runs.

B. Higher-order terms in the SPDC process

The output state of a SPDC process in the photon-number basis can be expressed as the product of the downconverted photons state $|\psi\rangle_{\text{SPDC}}$ and the pump photon state, where [5]

$$|\psi\rangle_{\text{SPDC}} \approx |\mathbb{0}\mathbb{0}\rangle + \epsilon|\mathbb{1}\mathbb{1}\rangle + \frac{\epsilon^2}{2}|\mathbb{2}\mathbb{2}\rangle + O(\epsilon^3). \tag{21}$$

Here $|n_s n_i\rangle$ represents the photon-number basis with the signal and idler photons n_s and n_i, respectively. The parameter ϵ is an overall efficiency related to the pump power, the nonlinear constant, and SPDC crystal thickness. Equation (21) shows the nondeterministic nature of these conventional photon sources, where ϵ determines the rate of producing single photons. Multiple-photon generation events usually contaminate the quantum state, and if the photon detector does not possess photon number resolution capabilities, we cannot distinguish between single- and few-photon detection.

To create three photons required for the experiment, two type-I SPDC sources are employed. The first one is supposed

[4]Here instead of sweeping ϕ in some increments in the entire interval $[0, 2\pi)$ and working out the ensemble averages over y and ϕ as in Eq. (1), the true phase is chosen randomly in that interval for each execution of the circuit. Then the resulting string $y \equiv \phi_0\phi_1\phi_2$ determines $\phi_{\text{est}}(y)$ according to Eq. (6). This leads to calculating one instance of the exponential term in Eq. (1). An ensemble average of sufficiently many instances yields the expression inside the modulus squared, which is used to compute the Holevo deviation.

to supply horizontally polarized single photons for mode "*a*" that are heralded by their partners in the trigger mode "*t*." The output state of this source can be written as

$$|\bar{\psi}_{at}\rangle \approx \left(1+\epsilon_1 \hat{a}_H^\dagger \hat{t}^\dagger + \frac{\epsilon_1^2}{2}\hat{a}_H^{\dagger 2}\hat{t}^{\dagger 2} + \frac{\epsilon_1^3}{6}\hat{a}_H^{\dagger 3}\hat{t}^{\dagger 3}\right)|\mathbb{0}\mathbb{0}\rangle, \tag{22}$$

where the overhead bar indicates that the resultant state contains multiphoton terms. Here, the terms higher than third order in ϵ_1 are discarded.

A second type-I SPDC source (composed of two sandwiched BiBO crystals with perpendicular optical axes) with overall efficiency ϵ_2 provides photons for modes "*b*" and "*c*" to realize the state $|\psi_{bc}\rangle$ given by Eq. (13). Preparing the pump photon in a linearly polarized state $\beta|H\rangle + \gamma|V\rangle$, where $|\beta|^2 + |\gamma|^2 = 1$, the state of downconverted photons can be described (up to second order in ϵ_2) by [39]

$$|\bar{\Xi}\rangle \approx \Big[1+\epsilon_2(\gamma\, \hat{b}_H^\dagger \hat{c}_H^\dagger + \beta\, \hat{b}_V^\dagger \hat{c}_V^\dagger) + \frac{\epsilon_2^2}{2}(\gamma\, \hat{b}_H^\dagger \hat{c}_H^\dagger + \beta\, \hat{b}_V^\dagger \hat{c}_V^\dagger)^2\Big]|\mathbb{0}\mathbb{0}\rangle. \tag{23}$$

The multiphoton state $|\bar{\Xi}\rangle$ needs to be converted into $|\bar{\psi}_{bc}\rangle$, for which the single-excitation terms form the desired state $|\psi_{bc}\rangle$ of Eq. (13). This can be achieved by subjecting $|\bar{\Xi}\rangle$ to further unitary evolution by means of two linear optical elements, which each implement a tunable beam splitter operation in a polarization basis on a specific mode "*m*,"

$$\hat{\mathfrak{U}}(\vartheta_m) = \exp[-i\vartheta_m(\hat{m}_H^\dagger \hat{m}_V + \hat{m}_H \hat{m}_V^\dagger)], \tag{24}$$

with $m = \{b, c\}$. The values for ϑ_b and ϑ_c are chosen so that one obtains

$$|\bar{\psi}_{bc}\rangle = \hat{\mathfrak{U}}(\vartheta_b)\,\hat{\mathfrak{U}}(\vartheta_c)\,|\bar{\Xi}\rangle. \tag{25}$$

Now, using Eqs. (22) and (25), the input state prior to the optimal state preparation gate is

$$|\bar{\psi}_{\rm in}\rangle = |\bar{\psi}_{at}\rangle|\bar{\psi}_{bc}\rangle, \tag{26}$$

where only three-photon amplitude terms $\epsilon_1\epsilon_2, \epsilon_1\epsilon_2^2, \epsilon_2\epsilon_1^2, \epsilon_1^3$ are used for post-selecting three-click coincidence detection, and higher-order amplitudes are neglected.

Applying this approach and assuming that optical modes perfectly overlap, numerical simulations of the phase measurement protocol can be accomplished through the same procedure as in the previous section. Before doing so, we need to determine two parameters ϵ_1 and ϵ_2 for the calculations. The overall efficiency of a pulsed SPDC source is related to its coincidence count rate $\mathfrak{C}$ via [40]

$$\epsilon = \sqrt{\frac{\mathfrak{C}}{\mathfrak{R}\,\lambda_{\rm i}\lambda_{\rm s}}}, \tag{27}$$

where $\mathfrak{R}$ is the pulsed laser repetition rate, and $\lambda_{\rm i}$ and $\lambda_{\rm s}$ are the heralding efficiency of the idler and signal modes. For the experiments conducted in this work, we found the overall efficiency approximately satisfying $\epsilon \in [0.05, 0.1]$. In particular, for the setting of 100 mW pump power, $\mathfrak{R} = 80$ MHz, $\lambda_{\rm i} \approx \lambda_{\rm s} = 13\%$, and $\mathfrak{C} \approx 5200$, we obtain $\epsilon \approx 0.06$. The result of computational modeling for the Holevo deviation $D_{\rm H}$ for varying ϵ_1 in the above interval while keeping $\epsilon_2 = 0.05$ is illustrated in Fig. 9(a). The detection efficiency is set at 13% as before. In Fig. 9(b), the roles of the two overall efficiencies are swapped.

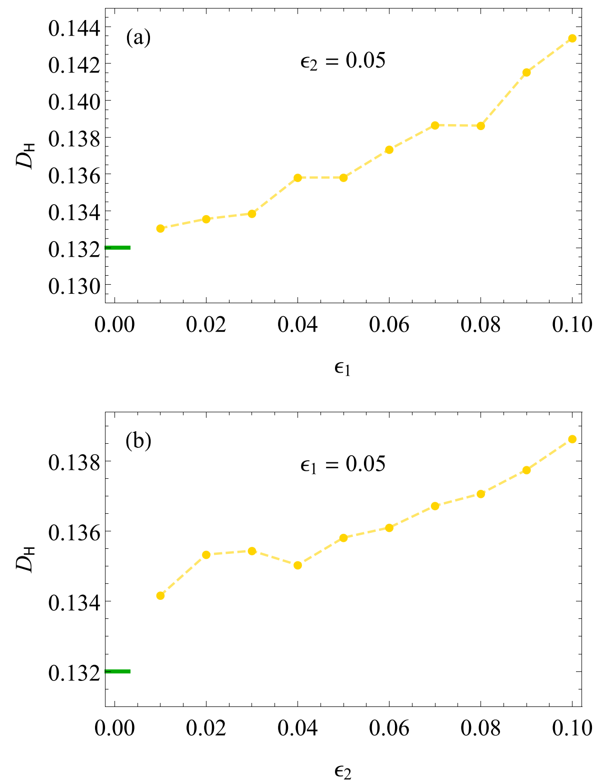

FIG. 9. The HPEA performance in the presence of higher-order terms in the SPDC process. The Holevo deviation, Eq. (1), is plotted by (a) varying the overall efficiency of the first SPDC source, while $\epsilon_2 = 0.05$, and (b) swapping the role of ϵ_1 and ϵ_2. The heralding efficiency is fixed at 13% for both plots. Each data point was obtained using 50×10^3 simulation runs.

Drawing a comparison between these plots and Fig. 8, it is obvious that optical mode mismatch would be expected to have a greater impact on the performance of the phase measurement scheme. As mentioned before, all of these experimental imperfections may be present at the same time. We avoided including them all together due to computational costs. However, in order to get a proper account of the real experimental situation, we will evaluate the protocol performance using the experimentally generated state, reconstructed via quantum state tomography.

IV. EXPERIMENTAL REALIZATION OF THE PROBE STATE

In this section, we present the experimental implementation of the optimal state creation. The experimental configuration is schematically shown in Fig. 10 consisting of three sections: the single-photon sources (blue panel), the entangling gate for preparing the optimal state (green panel), and quantum state tomography stages (gray panel). Two cascaded type-I SPDC sources (see Appendix E, and also described elsewhere [16]) are employed to supply photonic qubits encoded in the polarization degree of freedom. A single photon

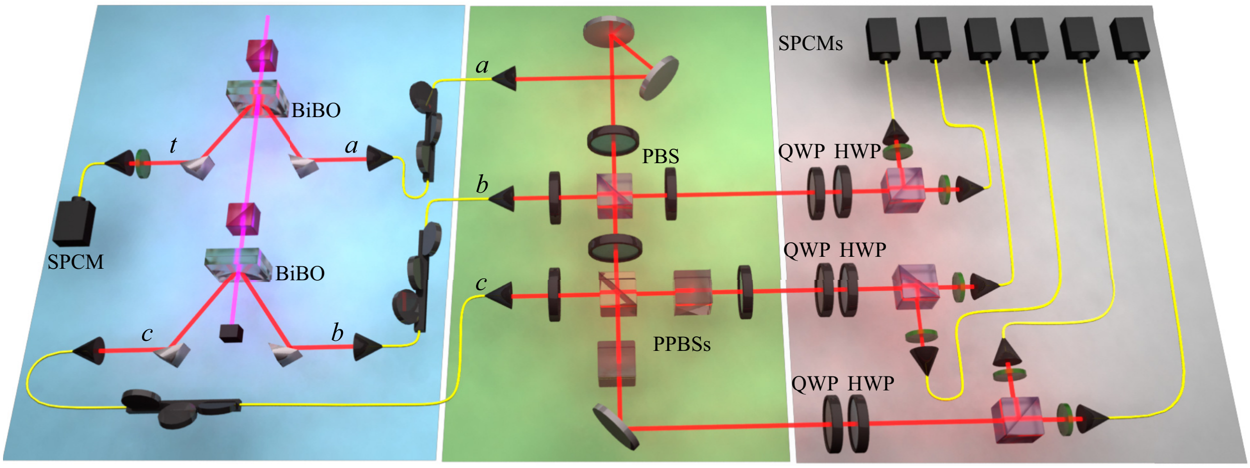

FIG. 10. Experimental setup arrangement. Blue region: Single and entangled photons at 820 nm are generated via two type-I SPDC sources. The SPDC crystals are pumped by pulsed UV light produced through a second-harmonic-generation process. Photons are guided using single-mode fibers into the entangling gate to create the optimal state. Green region: The desired probed state is post-selectively generated by realizing two entangling gates: the probabilistic nonuniversal CNOT gate acting between modes "a" and "b" composed of four HWPs and one PBS (equivalent to the red dashed box in Fig. 4), and the nondeterministic universal CNOT gate operating between modes "a" and "c" made up of three PPBSs where the central one (nonflipped) coherently combines the control and target photons and two HWPs set at 22.5° with respect to the optical axis (corresponding to the blue dashed box in Fig. 4). Gray region: quantum state reconstruction tomography stage. Photons are directed to polarization analysis units consisting of a QWP, HWP, and PBS followed by a 2 nm spectral filter and SPCM.

in mode "a" is heralded by its partner in the trigger detector produced by the first source. The second one generates a pair of entangled photons that are directed via fiber coupling towards modes "b" and "c" in the state preparation gate.

The NCN gate (red-dashed box in the circuit diagram in Fig. 4) is realized with a polarization beam splitter (PBS) and four half-waveplates (HWPs). The CN gate (blue-dashed box in the circuit diagram in Fig. 4) is made up of three partially polarized beam splitters (PPBSs) and two HWPs. The central PPBS has reflectivity $\eta_V = \frac{2}{3}$ and $\eta_H = 0$ for the vertically and horizontally polarized light, respectively. The other two PPBSs were flipped by 90° around the propagation direction of photons such that $\eta_V = 0$ and $\eta_H = \frac{2}{3}$; see Fig. 10. The two HWPs serve as 50:50 beam splitters of the polarization interferometer. A conceptual diagram of the HPEA is also shown in Fig. 15.

We saw in Sec. III A that high-quality quantum interference of photons is crucial for creating a state close to the optimal state, Eq. (10). This phenomenon takes place in our experiments between polarized photons in modes "a" and "b" incident on the PBS (in the NCN gate) and between photons in modes "a" and "c" impinging on the central PPBS (in the CN gate). Note that even though HOM interference occurs between two photons, the presence of these two is heralded by the other photon pair each from an independent SPDC source. This means fourfold coincidence counting, which leads to increasing the data collection time during which the setup should remain stable. The maximum interference visibility that can be obtained for a PBS is 1 and that of a PPBS with $\eta_V = \frac{2}{3}$ is 0.8 [16]. We have observed $\nu_{ab} = 0.97 \pm 0.03$ and $\nu_{ac} = 0.79 \pm 0.025$ visibility HOM interference, respectively; see Fig. 11.

Finally, to characterize the state, three-qubit polarization quantum state tomography was performed [41]. Figure 12(a) demonstrates the real and imaginary parts of $\rho_{\rm opt} = |\psi_{\rm opt}\rangle\langle\psi_{\rm opt}|$ calculated from Eq. (10). The result of reconstructed quantum state tomography $\rho_{\rm exp}$ using a maximum likelihood estimation technique is shown in Fig. 12(b). The state fidelity [42] with respect to $\rho_{\rm opt}$ was measured to be $F = 0.810 \pm 0.014$, and the state purity $\mathcal{P} = {\rm Tr}[\rho_{\rm exp}^2] = 0.75 \pm 0.02$. Uncertainties are estimated using a Monte Carlo numerical simulation, sampled from a Poisson distribution of photon counts. The measurements were taken at the low pump power setting to ensure a small, $\epsilon \approx 0.06$, probability amplitude of generating more than one photon pair from the same source. Together with a heralding efficiency of ≈0.13, characteristic for noncollinear SPDC sources, this resulted in

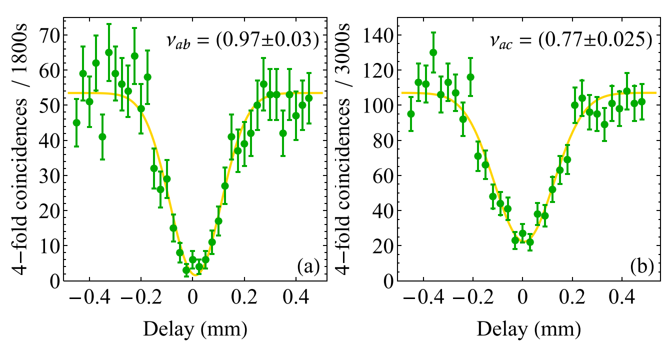

FIG. 11. Experimental HOM interference of photons produced via two independent SPDC sources. (a) Photons in modes "a" and "b" nonclassically interfere in the PBS; see Fig. 10. The observed visibility is $\nu = 0.97 \pm 0.03$, and the dip width is $229 \pm 19\,\mu$m. (b) Interference between photons in modes a and c in the central PPBS. The observed dip visibility is $\nu = 0.77 \pm 0.025$, and the dip width is $228 \pm 14\,\mu$m. See text for details.

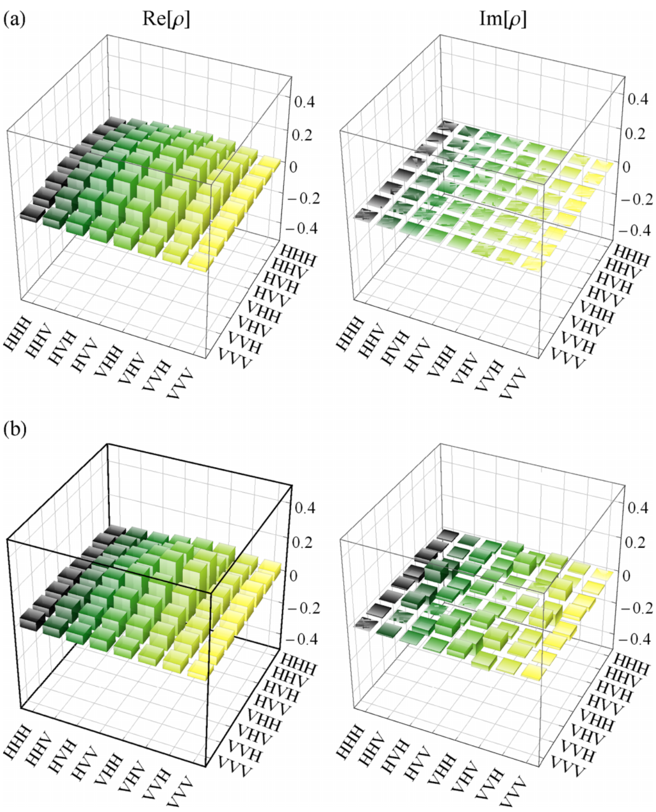

FIG. 12. (a) Real (left) and imaginary (right) parts of the state matrix $\rho_{\rm opt}$ reconstructed from polarization state tomography, and (b) the optimal state $\rho_{\rm exp} = |\psi_{\rm exp}\rangle\langle\psi_{\rm exp}|$, Eq. (10). The fidelity of the experimental state with respect to the optimal state is $F = 0.810 \pm 0.014$, and the purity is equal to $\mathcal{P} = 0.75 \pm 0.02$, calculated from approximately 4200 fourfold coincidence photodetection.

a low count rate, typically on the order of a few fourfold coincidences per minute. The overall state quality is comparable to (or better than) the states obtained by optical circuits that involve two CNOT gates and similar state generation technology (e.g., Ref. [43]).

We can test the expected performance of the obtained experimental state $\rho_{\rm exp}$ in the *ab initio* phase measurement protocol. To this end, numerical simulations of the algorithm were executed by replacing for the optimal state in the scheme and following the same recipe discussed in Sec. II E and Appendix B.[5] The results are illustrated in Fig. 13. The phase-dependent deviation $D_{\rm H}^{\phi}$ reveals the oscillatory behavior (green square markers) similar to the ideal state case, but unfortunately well above the SNL. After averaging over the true phase, the Holevo deviation is determined to be $D_{\rm H} = 0.445$ (blue horizontal line segment) compared to the SNL of 0.232 688.

[5]There is an exception here. The procedure outlined in Sec. II E has been formalized for the optimal state. However, as will be seen in Fig. 14, the reconstructed state tomography led to probability distributions that suggest $\phi_{\rm est}(y)$ are slightly shifted from those given in Eq. (6). The difference between any of the latter and the corresponding expression $\arg(\int P_{\phi_0\phi_1\phi_2} e^{i\phi} d\phi)$, where $P_{\phi_0\phi_1\phi_2}$ is the normalized probability distribution, results in a small shift.

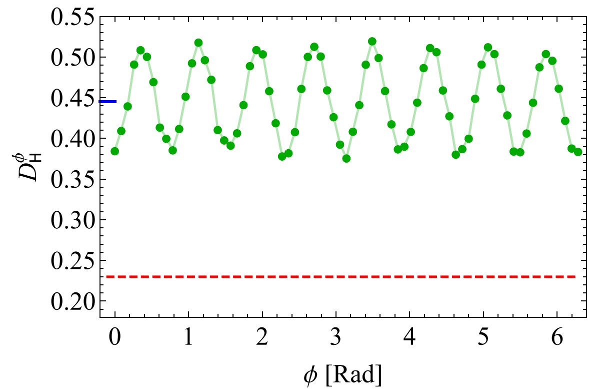

FIG. 13. Profile of the phase-dependent Holevo deviation, Eq. (18), as a function of phase for the experimental state $\rho_{\rm exp}$ (rectangular green points). The Holevo deviation, Eq. (3), is depicted by a blue horizontal line. The dashed red line illustrates the SNL as in Fig. 5.

These experimental results contrast with the predictions of our simulation results of Figs. 8 and 9, which show that for the achieved levels of mode overlap and high-order photon number noise, $\xi \approx 0.98$ and $\epsilon \approx 0.06$, the generated state should perform better than the SNL. The corresponding probability distribution of different measurement outcomes, Fig. 14, simulated using $\rho_{\rm exp}$ as input, shows a minor deviation of the function profile from the ideal bell-shaped curve and lower than expected maximum probability density. The small bump in the dotted curves suggests there should be a slight shift in the locus at which maximum probability occurs in comparison to those of the perfect case. As a result, the estimate $\phi_{\rm est}(y)$ should account for this slight difference with respect to values obtained from Eq. (6).

With this insight, we identify several causes for the discrepancy between the observed results and our theoretical prediction. First, our simulations were performed under the assumption that only a single source of noise was present, and they did not take into account the combined effect of both mode overlap and high-photon-number noise on the probe state quality. Second, the low levels of noise were achieved at the expense of an extremely low count rate due to low pump power and high loss from spectral filtering, leading to long measurement times. Although HOM interference demonstrated high mode overlap, this measurement was taken over a relatively (under 20 h) short time period. Three-qubit quantum state tomography lasted significantly longer (more than a week), leading to an inevitable HOM dip position shift, and degradation of quantum interference and overall optical setup alignment, impacting the probe state beyond what was predicted by the initial numerical simulation (see Appendix G for more details). Finally, despite generating a probe state of reasonably high quality in terms of noise, a systematic deviation from the ideal form of Eq. (10) would also degrade its performance in phase estimation by distorting the measurement outcome probability density functions from the ideal shape, as shown in Fig. 14. Such deviations are generally addressed through a calibration routine, consisting of iterations of measurements and setup adjustments. This approach was impractical in our case due to the very low

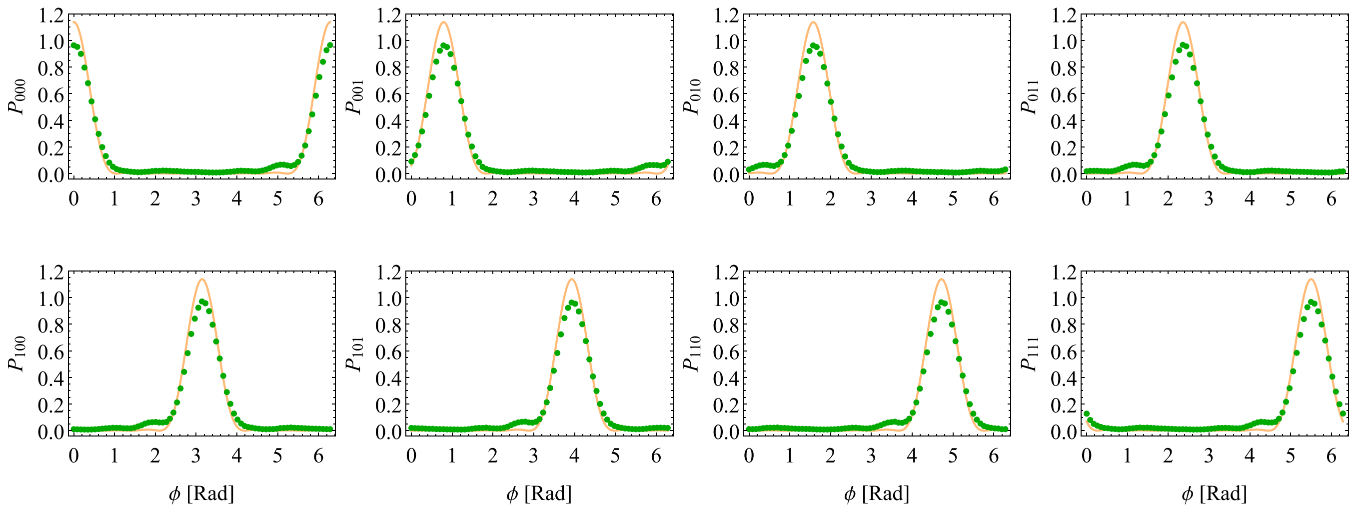

FIG. 14. (Normalized) probability distribution as in Fig. 6, but the green dots are simulation results using the reconstructed state $\rho_{\rm exp}$. The solid gold curves are obtained via Eq. (5) with the corresponding $\mathcal{C}_n$ for the HPEA. In all plots, $n_{\rm ens} = 50 \times 10^3$.

count rates. One way to overcome these challenges would be through increasing the count rates and time and frequency mode overlap by implementing novel efficient single-photon sources [44–46]. The same result cannot be simply achieved by boosting up the pump power as it would increase the probability of producing unwanted multiphoton pairs.

V. CONCLUSION

In summary, we studied a Heisenberg-limited interferometric phase estimation algorithm in the presence of experimental imperfections. Although, in principle, the protocol can exploit any physical qubit, our attention was concentrated on experimental realization using optical photons. Our optical scheme for preparation of the optimal three-photon $N = 7$ state included two probabilistic CNOT gates for which quantum interference of photons plays a pivotal role.

We numerically analyzed the effects of the two major expected experimental imperfections of the photonic setup: mode mismatch of the interfering photons, and multiphoton generation events in the photon sources. We found the impact of the former to be more severe than the latter. Nevertheless, we predicted that sub-SNL phase estimation should be possible in the presence of experimentally achievable levels of either type of imperfection, individually.

However, when we attempted to experimentally realize the optimal probe state, and characterized it by tomography, a numerical simulation of its use in phase estimation predicted a performance for phase estimation worse than the shot-noise limit. This discrepancy can perhaps be attributed to the fact that the necessary low levels of noise were achieved at the expense of very low count rates, which translate into long measurement duration, making it impractical to maintain the high quality of HOM interference for the entire duration of the tomography. This problem of stability would also likely affect the calibration of the state for the phase estimation protocol.

Nascent efficient photon sources, detection technology, and advances in integrated optics should be able to tackle this problem [46]. Upon overcoming this obstacle, future works can be directed towards implementing the full phase measurement circuit, which requires fast feedback control operations.

ACKNOWLEDGMENTS

The authors are indebted to Jian Li, formerly of the University of Science and Technology of China, for work on the state preparation protocol of Sec. II D. We also thank Raj B. Patel and Allen Boston for assistance with the data acquisition code, and Dominic W. Berry for useful discussions. This research was supported by the Australian Research Council Centre of Excellence Grants No. CE110001027 and No. CE170100012. S.D. acknowledges financial support through an Australian Government Research Training Program Scholarship and thanks the University of Western Australia.

APPENDIX A: OPTIMAL STATE GENERATION CIRCUIT

Consider a system comprised of linear optical components such as beam splitters, waveplates, etc. Assume M modes entering this network undergo a unitary transformation described by

$$\hat{\mathcal{U}}(G) = \exp[-i\,\hat{\mathbf{a}}^\dagger G\,\hat{\mathbf{a}}], \tag{A1}$$

where $\hat{\mathbf{a}} = (\hat{a}_1, \hat{a}_2, \dots, \hat{a}_M)^\top$ is a vector of annihilation operators, and G is a Hermitian matrix. Output modes are obtained in the Heisenberg picture according to

$$\hat{\mathcal{U}}^\dagger(G)\,\hat{\mathbf{a}}\,\hat{\mathcal{U}}(G) = S(G)\,\hat{\mathbf{a}}, \tag{A2}$$

where $S(G) = \exp[-iG]$ is the matrix representation of a unitary transformation induced on $\hat{\mathbf{a}}$. Let us now assume that the input state can be expressed by applying a function f of incoming modes into the system on the total vacuum state $|\mathbf{0}\rangle = |\mathbb{0}_1, \mathbb{0}_2, \dots, \mathbb{0}_M\rangle$ such that

$$|\psi_{\rm in}\rangle = f(\hat{a}_1^\dagger, \hat{a}_2^\dagger, \dots, \hat{a}_M^\dagger)|\mathbf{0}\rangle. \tag{A3}$$

The output state is simply obtained by unitarily evolving the above state, that is, $|\psi_{\text{out}}\rangle = \hat{\mathcal{U}}(G)|\psi_{\text{in}}\rangle$. It is straightforward to expand out this last relation using Eq. (A2) and the fact that $\hat{\mathcal{U}}^\dagger(G) = \hat{\mathcal{U}}(-G)$ and $S^\dagger(G) = S(-G)$ to get the following form:

$$|\psi_{\text{out}}\rangle = f(\hat{\mathbf{a}}^\dagger S_{:1}, \hat{\mathbf{a}}^\dagger S_{:2}, \dots, \hat{\mathbf{a}}^\dagger S_{:M})|\mathbf{0}\rangle, \tag{A4}$$

where $S_{:m}$ denotes the mth column of the matrix S, and $\hat{\mathbf{a}}^\dagger = (\hat{a}_1^\dagger, \hat{a}_2^\dagger, \dots, \hat{a}_M^\dagger)$. Finding the matrix S is thus central in our calculations to determine the output state of a quantum circuit composed of linear optical elements.

Let us now investigate how the two entangling gates produce the optimal state. With the input state $|\psi_{bc}\rangle$ the same as in Eq. (13) and $|\psi_a\rangle = |H\rangle$, we obtain

$$\left|\psi_{\text{in}}^{\text{NCN}}\right\rangle = f(\hat{v}_a^\dagger, \hat{a}_V^\dagger, \hat{a}_H^\dagger, \hat{b}_H^\dagger, \hat{b}_V^\dagger, \hat{c}_V^\dagger, \hat{c}_H^\dagger, \hat{v}_c^\dagger)|\mathbf{0}\rangle, \tag{A5}$$

$$= (\alpha_0\, \hat{a}_H^\dagger \hat{b}_H^\dagger \hat{c}_H^\dagger + \alpha_1\, \hat{a}_H^\dagger \hat{b}_H^\dagger \hat{c}_V^\dagger + \alpha_2\, \hat{a}_H^\dagger \hat{b}_V^\dagger \hat{c}_H^\dagger + \alpha_3\, \hat{a}_H^\dagger \hat{b}_V^\dagger \hat{c}_V^\dagger)\, |\mathbf{0}\rangle. \tag{A6}$$

Note that the vacuum modes may be removed from the calculations as they are relevant for the second CNOT gate operation. The next step involves constructing the corresponding S^{NCN} matrix by multiplying matrices describing different optical components affecting appropriate modes; here four BSs and one mode-swapping operation while leaving modes c_V and c_H unchanged. This process leads to

$$S^{\text{NCN}} = \begin{pmatrix} 1 & 0 & 0 & 0 & 0 & 0 & 0 & 0 \\ 0 & \eta_1 & \sqrt{\eta_1(1-\eta_1)} & -\sqrt{\eta_1(1-\eta_1)} & 1-\eta_1 & 0 & 0 & 0 \\ 0 & \sqrt{\eta_1(1-\eta_1)} & 1-\eta_1 & \eta_1 & -\sqrt{\eta_1(1-\eta_1)} & 0 & 0 & 0 \\ 0 & -\sqrt{\eta_1(1-\eta_1)} & \eta_1 & 1-\eta_1 & \sqrt{\eta_1(1-\eta_1)} & 0 & 0 & 0 \\ 0 & 1-\eta_1 & -\sqrt{\eta_1(1-\eta_1)} & \sqrt{\eta_1(1-\eta_1)} & 1-\eta_1 & 0 & 0 & 0 \\ 0 & 0 & 0 & 0 & 0 & 1 & 0 & 0 \\ 0 & 0 & 0 & 0 & 0 & 0 & 1 & 0 \\ 0 & 0 & 0 & 0 & 0 & 0 & 0 & 1 \end{pmatrix}, \tag{A7}$$

where the same mode ordering as the one appearing in the argument of function f in Eq. (A5) is employed for the matrix representation. Now using Eq. (A4), the total output state after applying the first CNOT gate becomes

$$\left|\psi_{\text{out}}^{\text{NCN}}\right\rangle = f\big(\hat{\mathbf{a}}^\dagger S_{:1}^{\text{NCN}}, \dots, \hat{\mathbf{a}}^\dagger S_{:8}^{\text{NCN}}\big)|\mathbf{0}\rangle \tag{A8}$$

$$= \big[\alpha_0\big(\hat{\mathbf{a}}^\dagger S_{:3}^{\text{NCN}}\big)\big(\hat{\mathbf{a}}^\dagger S_{:4}^{\text{NCN}}\big)\big(\hat{\mathbf{a}}^\dagger S_{:7}^{\text{NCN}}\big) + \alpha_1\big(\hat{\mathbf{a}}^\dagger S_{:3}^{\text{NCN}}\big)\big(\hat{\mathbf{a}}^\dagger S_{:4}^{\text{NCN}}\big)\big(\hat{\mathbf{a}}^\dagger S_{:6}^{\text{NCN}}\big) + \alpha_2\big(\hat{\mathbf{a}}^\dagger S_{:3}^{\text{NCN}}\big)\big(\hat{\mathbf{a}}^\dagger S_{:5}^{\text{NCN}}\big)\big(\hat{\mathbf{a}}^\dagger S_{:7}^{\text{NCN}}\big)$$
$$+ \alpha_3\big(\hat{\mathbf{a}}^\dagger S_{:3}^{\text{NCN}}\big)\big(\hat{\mathbf{a}}^\dagger S_{:5}^{\text{NCN}}\big)\big(\hat{\mathbf{a}}^\dagger S_{:6}^{\text{NCN}}\big)\big]\, |\mathbf{0}\rangle$$

$$= \frac{1}{\sqrt{2}}(|\psi_1\rangle + |\psi_d\rangle), \tag{A9}$$

where

$$\hat{\mathbf{a}}^\dagger = (\hat{v}_a^\dagger, \hat{a}_V^\dagger, \hat{a}_H^\dagger, \hat{b}_H^\dagger, \hat{b}_V^\dagger, \hat{c}_V^\dagger, \hat{c}_H^\dagger, \hat{v}_c^\dagger), \tag{A10}$$

and $|\psi_d\rangle$ represents a superposition of states with more than one photon in either of the qubit's modes.

The final output state from the circuit diagram shown in Fig. 4 is calculated by setting the input state entering the CN gate as

$$\left|\psi_{\text{in}}^{\text{CN}}\right\rangle = \left|\psi_{\text{out}}^{\text{NCN}}\right\rangle \tag{A11}$$

$$= g(\hat{v}_a^\dagger, \hat{a}_V^\dagger, \hat{a}_H^\dagger, \hat{b}_H^\dagger, \hat{b}_V^\dagger, \hat{c}_V^\dagger, \hat{c}_H^\dagger, \hat{v}_c^\dagger)|\mathbf{0}\rangle, \tag{A12}$$

and applying the corresponding matrix S^{CN}, which is

$$S^{\text{CN}} = \begin{pmatrix} -\sqrt{\eta_2} & \sqrt{(1-\eta_2)} & 0 & 0 & 0 & 0 & 0 & 0 \\ \sqrt{1-\eta_1} & \sqrt{\eta_2} & 0 & 0 & 0 & 0 & 0 & 0 \\ 0 & 0 & -\sqrt{\eta_2} & -\sqrt{\eta_1(1-\eta_1)} & \sqrt{(1-\eta_1)(1-\eta_2)} & 0 & 0 & 0 \\ 0 & 0 & 0 & 1 & 0 & 0 & 0 & 0 \\ 0 & 0 & 0 & 0 & 1 & 0 & 0 & 0 \\ 0 & 0 & \sqrt{\eta_1(1-\eta_2)} & (1-2\eta_1)\sqrt{\eta_2} & 2\sqrt{\eta_1\eta_2(1-\eta_1)} & \sqrt{(1-\eta_1)(1-\eta_2)} & 0 & 0 \\ 0 & 0 & \sqrt{(1-\eta_1)(1-\eta_2)} & 2\sqrt{\eta_1\eta_2(1-\eta_1)} & (1-2\eta_1)\sqrt{\eta_2} & -\sqrt{\eta_1(1-\eta_2)} & 0 & 0 \\ 0 & 0 & 0 & \sqrt{(1-\eta_1)(1-\eta_2)} & \sqrt{\eta_1(1-\eta_2)} & -\sqrt{\eta_2} & 0 & 0 \end{pmatrix}, \tag{A13}$$

to obtain

$$|\psi_{\text{out}}^{\text{CN}}\rangle = g\big(\hat{\mathbf{a}}^{\dagger}S_{:1}^{\text{CN}}, \dots, \hat{\mathbf{a}}^{\dagger}S_{:8}^{\text{CN}}\big)|\mathbf{0}\rangle, \tag{A14}$$

$$= \frac{1}{\sqrt{18}}|\psi_{\text{opt}}\rangle + |\chi_d\rangle. \tag{A15}$$

Here the function g can be found via Eq. (A9), and $|\chi_d\rangle$ contains states with at least two photons in a single polarization or vacuum mode.

APPENDIX B: PHASE MEASUREMENT CIRCUIT

Consider the Heisenberg-limited phase estimation scheme with $K+1=3$ photons. Let us assume the input state is represented by ρ_{in}. Recalling the circuit shown in Fig. 2, the state $\rho^{(K)} \in \mathbb{B}^{2^{K+1}}$ of the system before the first X-measurement on the Kth photon is

$$\rho^{(K)} = \left(\hat{U}^{2^K}\bigotimes_{k=1}^{K}\hat{I}\right)\rho_{\text{in}}\left(\hat{U}^{2^K}\bigotimes_{k=1}^{K}\hat{I}\right)^{\dagger}, \tag{B1}$$

where

$$\hat{U}^m = \begin{pmatrix}1 & 0\\ 0 & e^{im\phi}\end{pmatrix}, \quad \hat{I} = \begin{pmatrix}1 & 0\\ 0 & 1\end{pmatrix}. \tag{B2}$$

Here ϕ is the unknown phase shift. The result of the X-measurement on the Kth photon is determined by the following measurement operators:

$$\hat{\mathcal{M}}_r^{(K)} = \hat{\Pi}_r\bigotimes_{k=1}^{K}\hat{I}, \tag{B3}$$

where $r \in \{+,-\}$ is a measurement result, and $\hat{\Pi}_r = |r\rangle\langle r|$ is the projection operator onto the X basis of the Kth photon. Therefore, the probability of finding the Kth photon in one of the X bases is

$$\wp_r^{(K)} = \text{Tr}\big[\rho^{(K)}\hat{\mathcal{M}}_r^{(K)\dagger}\hat{\mathcal{M}}_r^{(K)}\big] = \text{Tr}\big[\rho^{(K)}\hat{\mathcal{M}}_r^{(K)}\big]. \tag{B4}$$

Stochastic numerical simulations determine if the Kth photon is found in either of $|\pm\rangle$. Depending on the result of this measurement, the conditional system state $\rho_r^{(K)}$ after the measurement on the Kth photon is found via quantum measurement theory given by [1,47]

$$\rho_r^{(K)} = \big[\hat{\mathcal{M}}_r^{(K)}\rho^{(K)}\hat{\mathcal{M}}_r^{(K)\dagger}\big]/\wp_r^{(K)} = \hat{\Pi}_r \otimes \rho_r^{(K-1)}, \tag{B5}$$

where $\rho_r^{(K-1)} \in \mathbb{B}^{2^K}$ is the reduced state matrix of the other remaining K photons. The next step of the protocol includes some control operation depending on the result of the previous read out. That is, the measurement result $r = +(-)$ corresponds to the feedback "OFF(ON)" setting. Thus, in the reduced-dimension Hilbert space of the system, the state matrix before the measurement on the $(K-1)$th photon when the control operation is ON can be written as

$$\rho^{(K-1)} = V^{(K-1)}\rho_r^{(K-1)}V^{(K-1)\dagger}, \tag{B6}$$

where

$$V^{(K-1)} \equiv \left[\hat{U}^{2^{K-1}}R\left(\frac{\pi}{2}\right)\right]\bigotimes_{k=2}^{K}R\left(\frac{\pi}{2^k}\right), \tag{B7}$$

$$R(\theta) = \begin{pmatrix}e^{i\theta/2} & 0\\ 0 & e^{-i\theta/2}\end{pmatrix}, \tag{B8}$$

and if the control operation is OFF, the state matrix is

$$\rho^{(K-1)} = \left(\hat{U}^{2^{K-1}}\bigotimes_{k=1}^{K}\hat{I}\right)\rho_r^{(K-1)}\left(\hat{U}^{2^{K-1}}\bigotimes_{k=1}^{K}\hat{I}\right)^{\dagger}. \tag{B9}$$

Using the same procedure, the measurement on the $(K-1)$th photon is described. In other words, by changing $K \to K-1$ we can recall Eqs. (B3)–(B9) to obtain the measurement outcome and the reduced state $\rho_r^{(K-2)} \in \mathbb{B}^{2^{K-1}}$ of the system. These steps are repeated for each photon until the zeroth one, for which the measurement operator is simply the projector $\hat{\mathcal{M}}_r^{(0)} = \hat{\Pi}_r$.

APPENDIX C: CALCULATIONS OF THE SHOT-NOISE LIMIT

Consider the interferometer illustrated in Fig. 1 with $p=1$. In an ideal experimental scenario in which a single photon is incident into one arm of the interferometer, the probability of detecting a photon in either of the outputs ports is

$$p(u|\phi,\theta) = \tfrac{1}{2}[1 + u\cos(\phi-\theta)], \tag{C1}$$

where $u \in \{-1, 1\}$ is the measurement result. Assuming that m measurement outcomes are obtained, one can define a vector $\mathbf{u}_m = \{u_1, u_2, \dots, u_m\}$ in which each u_ℓ is defined as above. Therefore, the probability for the series of measurement results is

$$p(\mathbf{u}_m|\phi,\boldsymbol{\theta}) = \tfrac{1}{2}[1 + u\cos(\phi-\theta)], \tag{C2}$$

where $\boldsymbol{\theta} = \{\theta_1, \theta_2, \dots, \theta_m\}$ are the measurement angles for each photon. The Holevo variance in the phase estimate is $V_H = \mu^{-2} - 1$, where $\mu = |\langle e^{i\phi}\rangle|$, and using the above probability distribution it can be expressed as

$$\mu = \frac{1}{2\pi}\sum_{\mathbf{u}_m}\left|\int d\phi\, e^{i\phi}\, p(\mathbf{u}_m|\phi,\boldsymbol{\theta})\right|. \tag{C3}$$

Calculating this integral for a small number of resources ($N = 3, 7$), one can obtain the SNL for Holevo variance. While these solutions are not unique, we find that setting $\boldsymbol{\theta} = \{0, 0, \pi/2\}$ rad would achieve $V_{\text{SNL}} = 0.655\,845\dots$ for an $N=3$ measurement, while the measurement angles $\boldsymbol{\theta} = \{0,\ 0,\ 2.310\,99, 1.321\,33,\ 1.321\,33,\ 0.843\,774,\ -0.830\,605\}$ rad would achieve $V_{\text{SNL}} = 0.232\,688\dots$ for an $N=7$ measurement.

APPENDIX D: HOM VISIBILITY AND SPATIAL OPTICAL MODE MISMATCH

Recalling Eq. (19), the probability for observing a coincidence photon detection is

$$\begin{aligned} p_{\text{coin}} &= \langle \hat{n}_{a_D}\hat{n}_{b_D}\rangle \\ &= \langle \mathbf{01}|(\hat{n}_{\hat{v}_2^\circ} + \hat{n}_{\hat{a}^\circ} + \hat{n}_{\hat{v}_1^\circ})(\hat{n}_{\hat{v}_4^\circ} + \hat{n}_{\hat{b}^\circ} + \hat{n}_{\hat{v}_3^\circ})|\mathbf{01}\rangle, \end{aligned} \tag{D1}$$

where

$$|\mathbf{01}\rangle \equiv |\mathbb{0}\rangle_{\hat{v}_1^\circ} \otimes |\mathbb{0}\rangle_{\hat{v}_2^\circ} \otimes |\mathbb{0}\rangle_{\hat{v}_3^\circ} \otimes |\mathbb{0}\rangle_{\hat{v}_4^\circ} \otimes |\mathbb{1}\rangle_{\hat{a}^\circ} \otimes |\mathbb{1}\rangle_{\hat{b}^\circ}. \tag{D2}$$

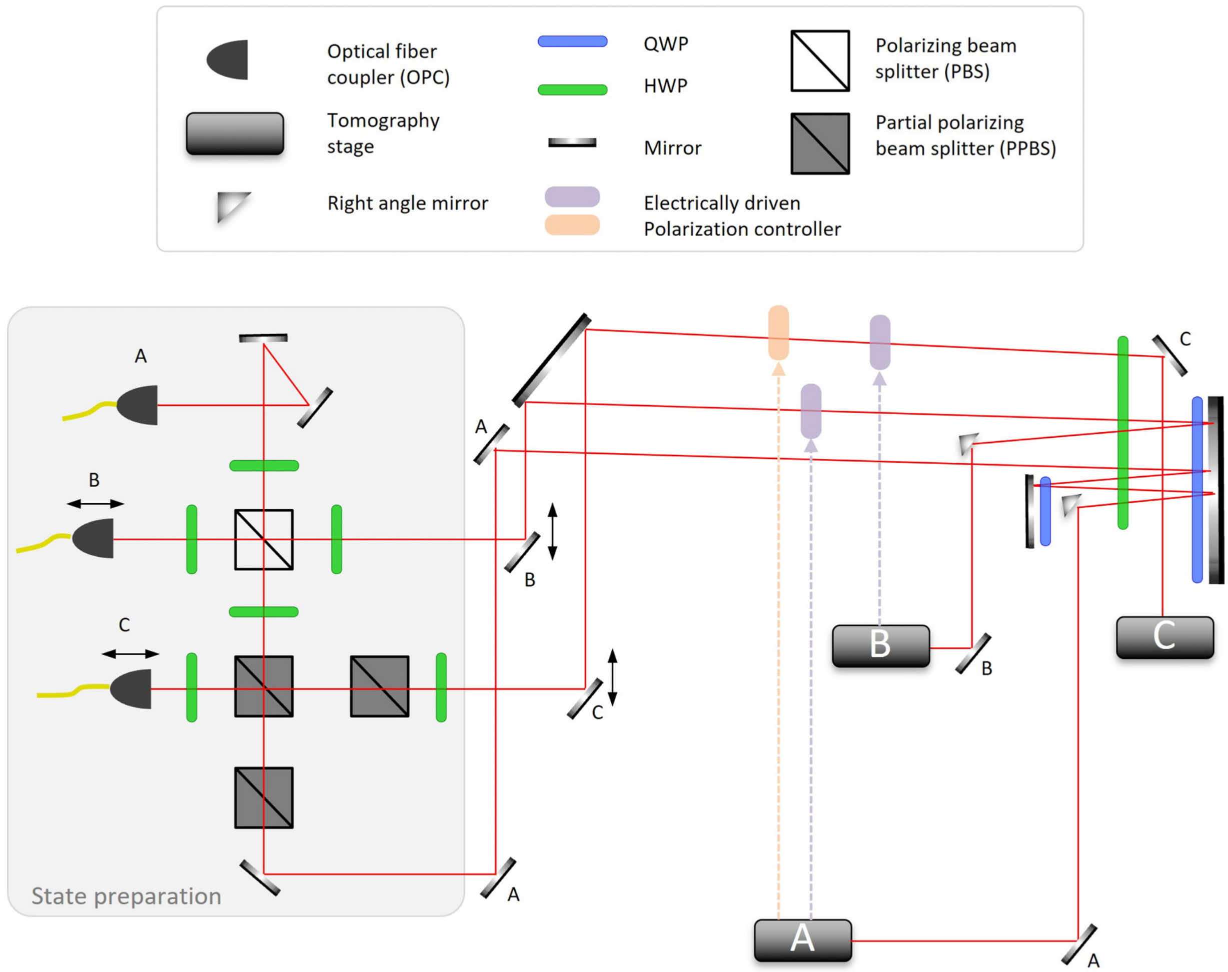

FIG. 15. A diagram of the Heisenberg-limited phase estimation algorithm with $N = 7$ resources. The gray panel depicts the optimal state generation as in Fig. 10. The rest shows applications of phase shift gate (large green HWP) and classical conditional control operations (shown by orange and purple boxes for rotation by $\pi/4$ and $\pi/2$, respectively).

We use superscript "o" to denote output modes corresponding to the relevant input modes. There are nine terms that should be calculated separately to obtain a relation for the probability as a function of mode mismatch parameters. It is straightforward to show that the output modes are given by the following equations:

$$\hat{v}_1^o = \sqrt{(1-\eta)(1-\xi_2)}\,\hat{b} - \sqrt{\xi_2(1-\eta)}\,\hat{v}_4 - \sqrt{\eta}\,\hat{v}_1, \tag{D3a}$$

$$\hat{a}^o = \sqrt{(1-\eta)(1-\xi_2)}\,\hat{v}_4 + \sqrt{\xi_2(1-\eta)}\,\hat{b} - \sqrt{\eta(1-\xi_1)}\,\hat{v}_2 - \sqrt{\eta\xi_1}\,\hat{a}, \tag{D3b}$$

$$\hat{v}_2^o = \sqrt{1-\eta}\,\hat{v}_3 - \sqrt{\eta(1-\xi_1)}\,\hat{a} + \sqrt{\eta\xi_1}\,\hat{v}_2, \tag{D3c}$$

$$\hat{v}_3^o = \sqrt{(1-\eta)(1-\xi_1)}\,\hat{a} - \sqrt{\xi_1(1-\eta)}\hat{v}_2 + \sqrt{\eta}\hat{v}_3, \tag{D3d}$$

$$\hat{b}^o = \sqrt{(1-\eta)(1-\xi_1)}\,\hat{v}_2 + \sqrt{\xi_1(1-\eta)}\,\hat{a} + \sqrt{\eta(1-\xi_2)}\,\hat{v}_4 - \sqrt{\eta\xi_2}\,\hat{b}, \tag{D3e}$$

$$\hat{v}_4^o = \sqrt{(1-\eta)}\,\hat{v}_1 + \sqrt{\eta(1-\xi_2)}\,\hat{b} - \sqrt{\eta\xi_2}\hat{v}_4. \tag{D3f}$$

Now by using these equations and the commutation relations for creation and annihilation operators of each mode, all terms in Eq. (D1) can be calculated in a straightforward manner. For instance, the first term is equal to

$$\begin{aligned}
&\langle \mathbf{01}|\hat{n}_{\hat{v}_2^o}\hat{n}_{\hat{v}_4^o}|\mathbf{01}\rangle \\
&= \langle \mathbf{01}|\ \hat{v}_2^{o\dagger}\hat{v}_2^o\hat{v}_4^{o\dagger}\hat{v}_4^o\ |\mathbf{01}\rangle, \\
&= \langle \mathbf{01}|[\sqrt{1-\eta}\,\hat{v}_3^\dagger - \sqrt{\eta(1-\xi_1)}\,\hat{a}^\dagger + \sqrt{\eta\xi_1}\,\hat{v}_2^\dagger] \\
&\quad \times [\sqrt{1-\eta}\,\hat{v}_3 - \sqrt{\eta(1-\xi_1)}\,\hat{a} + \sqrt{\eta\xi_1}\,\hat{v}_2] \\
&\quad \times [\sqrt{(1-\eta)}\,\hat{v}_1^\dagger + \sqrt{\eta(1-\xi_2)}\,\hat{b}^\dagger - \sqrt{\eta\xi_2}\hat{v}_4^\dagger] \\
&\quad \times [\sqrt{(1-\eta)}\,\hat{v}_1 + \sqrt{\eta(1-\xi_2)}\,\hat{b} - \sqrt{\eta\xi_2}\hat{v}_4]|\mathbf{01}\rangle, \\
&= [\eta^2(1-\xi_1)(1-\xi_2)]\langle \mathbf{1}|\hat{a}^\dagger\hat{a}\,\hat{b}^\dagger\hat{b}|\mathbf{1}\rangle, \\
&= \eta^2(1-\xi_1)(1-\xi_2),
\end{aligned} \tag{D4}$$

where $|\mathbf{1}\rangle = |1\rangle_{\hat{a}^o} \otimes |1\rangle_{\hat{b}^o}$, and in the second to last line we just kept nonzero terms. Applying the same procedure to the rest of the terms in Eq. (D1) gives

$$\langle \mathbf{01}|\hat{n}_{\hat{v}_2^o}\hat{n}_{\hat{b}^o}|\mathbf{01}\rangle = \eta^2\,\xi_2\,(1-\xi_1), \tag{D5a}$$

$$\langle \mathbf{01}|\hat{n}_{\hat{v}_2^o}\hat{n}_{\hat{v}_3^o}|\mathbf{01}\rangle = 0, \tag{D5b}$$

$$\langle \mathbf{01}|\hat{n}_{\hat{a}^o}\hat{n}_{\hat{v}_4^o}|\mathbf{01}\rangle = \eta^2\,\xi_1\,(1-\xi_2), \tag{D5c}$$

$$\langle \mathbf{01}|\hat{n}_{\hat{a}^o}\hat{n}_{\hat{b}^o}|\mathbf{01}\rangle = \xi_1\xi_2[1-4\eta(1-\eta)], \tag{D5d}$$

$$\langle \mathbf{01}|\hat{n}_{\hat{a}^o}\hat{n}_{\hat{v}_3^o}|\mathbf{01}\rangle = (1-\eta)^2\,\xi_2\,(1-\xi_1), \tag{D5e}$$

$$\langle \mathbf{01}|\hat{n}_{\hat{v}_1^o}\hat{n}_{\hat{v}_4^o}|\mathbf{01}\rangle = 0, \tag{D5f}$$

$$\langle \mathbf{01}|\hat{n}_{\hat{v}_1^o}\hat{n}_{\hat{b}^o}|\mathbf{01}\rangle = (1-\eta)^2\,\xi_1\,(1-\xi_2), \tag{D5g}$$

$$\langle \mathbf{01}|\hat{n}_{\hat{v}_1^o}\hat{n}_{\hat{v}_3^o}|\mathbf{01}\rangle = (1-\eta)^2\,(1-\xi_1)(1-\xi_2). \tag{D5h}$$

Summing up all of these terms gives Eq. (19),

$$p_{\text{coin}} = \langle \hat{n}_{a_D}\hat{n}_{b_D}\rangle = \tfrac{1}{2}(1-\xi_1\xi_2). \tag{D6}$$

The dip visibility can easily be worked out now once we have the probability of coincidence detection.

APPENDIX E: PHOTON SOURCES

Photons required for conducting the experiments produced via two type-I spontaneous parametric downconversion processes. A mode-locked *Tsunami* pulsed laser—which uses a titanium-doped sapphire solid-state laser medium and with a central frequency at 820 nm and a pulse duration of approximately 125 fs—was employed to generate upconverted photons at 410 nm through the second-harmonic-generation (SHG) phenomenon using a 2 mm lithium triborate (LBO) crystal. This SHG beam was collimated with a $f = 75$ mm lens and the infrared pump was spatially filtered away using two dispersive prisms. To suppress the residual red light, two short-pass dichroic mirrors with 98% reflectivity are used. To adjust the brightness and polarization of the infrared light, the LBO crystal was preceded with two HWPs and a linear polarizer in between. For the first SPDC process the ultraviolet light was first passed through a linear polarizer and HWP (to allow for adjusting the incident photons polarization) and then focused onto a 0.5 mm bismuth borate (BiBO) crystal using an $f = 400$ mm lens. A similar arrangement was also employed for setting up the second SPDC source. However, here we used a paired BiBO crystal in order to create an entangled state as in Eq. (13). This means both crystals should be pumped and as a result the two overlapping cones of downconverted photons should efficiently and symmetrically be collected. This can be achieved by adjusting the sandwiched crystals for phase matching and using a precompensating crystal to erase the time information (the first crystal produces horizontally polarized photons, and the second one generates vertically polarized photons at a later time).

APPENDIX F: SCHEMATIC OF $N = 7$ HPEA

A conceptual diagram of the three-photon interferometric phase estimation is shown in Fig. 15. The gray area is the state preparation stage where it is analyzed in Sec. IV. According to the quantum circuit of the HPEA, Fig. 2, the photon in mode "a" undergoes 2^2 applications of the phase shift prior to projection onto the X basis. Conditioned on the measurement outcome, unitary operations $R(\pi/2)$ and $R(\pi/4)$ are applied to photons in modes "b" and "c" (shown by the purple and orange oval boxes), respectively. Afterwards, the photon in mode "b" phase-shifted 2^1 times before being measured in the X basis. The result of this measurement determines whether or not rotation $R(\pi/2)$ should be applied to the photon in mode "c." The latter experiences only 2^0 application of $\hat{U}$ before measurement.

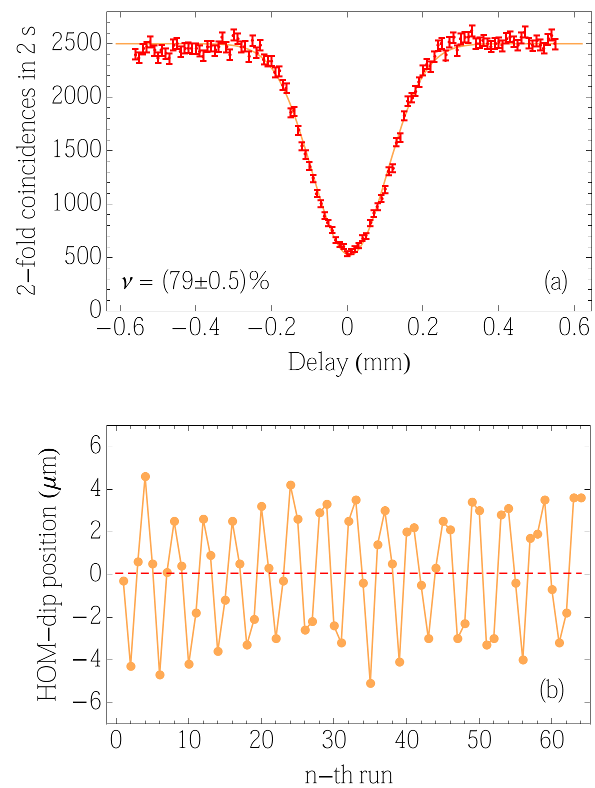

FIG. 16. Experimental HOM interference of two dependent photons. (a) A photon in one mode interferes with a photon in the other mode in the PPBS of the probabilistic universal CNOT gate. The visibility is $(79 \pm 0 : 5)\%$, and the dip width is 234 ± 5 μm. (b) Shows fluctuations in the position of the HOM-dip. We repeated the same experiment some 60 times where each took 600 s. A maximum deviation of 5 μm around the average was observed.

APPENDIX G: HOM INTERFERENCE ANALYSIS

We have experimentally run a series of HOM interference phenomena between photons that originated from the single SPDC source. For a nondeterministic universal CNOT gate setup (as in Fig. 10 with the difference that photons in modes "a" and "c" are produced independent of each other), the dip visibility ideally is 80%. For twofold coincidences (2500 events collected at the baseline within 2 s) we measured $v = (79 \pm 0.5)\%$ with the coherence length of approximately well above 200 μm, Fig. 16(a). The oscillatory behavior of HOM-dip position for successive runs of the same experiment (which each took almost 10 min) shows a maximum deviation of 5 μm, Fig. 16(b). For this particular scenario with a rather large coherence length, the dip position variation can be neglected. However, in this work we characterize our photons source by measuring fourfold coincidences (detection of approximately 4×10^{-2} successful events at the baseline within 2 s). That figure is even smaller for the probabilistic nonuniversal CNOT gate operation (interference of photons between mode "a" and "b" in Fig. 10). This analysis leads us to conclude that over the course of reconstructing state tomography, the quality of quantum interference should have significantly degraded for the purpose of Heisenberg-limited phase estimation.

[1] H. M. Wiseman and G. J. Milburn, *Quantum Measurement and Control* (Cambridge University Press, Cambridge, 2009).
[2] K. Jacobs, *Quantum Measurement Theory and Its Applications* (Cambridge University Press, Cambridge, 2014).
[3] V. Giovannetti, S. Lloyd, and L. Maccone, Nat. Photon. **5**, 222 (2011).
[4] S. Pirandola, B. R. Bardhan, T. Gehring, C. Weedbrook, and S. Lloyd, Nat. Photon. **12**, 724 (2018).
[5] A. Christ, A. Fedrizzi, H. Hübel, T. Jennewein, and C. Silberhorn, in *Single-photon Generation and Detection*, edited by A. Migdall, S. Polyakov, J. Fan, and J. Bienfang (Elsevier, Amsterdam, 2013), pp. 352–401.
[6] T. Nagata, R. Okamoto, J. L. O'Brien, K. Sasaki, and S. Takeuchi, Science **316**, 726 (2007).
[7] J. P. Dowling, Contemp. Phys. **49**, 125 (2008).
[8] H. Yonezawa, D. Nakane, T. A. Wheatle, H. M. Wiseman, E. H. Huntington, and A. Furusawa, Science **337**, 1514 (2012).
[9] S. Slussarenko, M. M. Weston, H. M. Chrzanowski, L. K. Shalm, V. B. Verma, S. W. Nam, and G. J. Pryde, Nat. Photon. **11**, 700 (2017).
[10] G. S. Thekkadath, M. E. Mycroft, B. A. Bell, C. G. Wade, A. Eckstein, D. S. Phillips, R. B. Patel, A. Buraczewski, A. E. Lita, T. Gerrits, S. W. Nam, M. Stobińska, A. I. Lvovsky, and I. A. Walmsley, npj Quantum Inf. **6**, 89 (2020).
[11] C. You, M. Hong, P. Bierhorst, A. E. Lita, S. Glancy, S. Kolthammer, E. Knill, S. W. Nam, R. P. Mirin, O. S. Magaña-Loaiza, and T. Gerrits, Appl. Phys. Rev. **8**, 041406 (2021).
[12] B. L. Higgins, D. W. Berry, S. D. Bartlett, H. M. Wiseman, and G. J. Pryde, Nature (London) **450**, 393 (2007).
[13] G. Y. Xiang, B. L. Higgins, D. W. Berry, H. M. Wiseman, and G. J. Pryde, Nat. Photon. **5**, 43 (2011).
[14] A. A. Berni, T. Gehring, B. M. Nielsen, V. Händchen, M. G. A. Paris, and U. L. Andersen, Nat. Photon. **9**, 577 (2015).
[15] M. Hassani, C. Macchiavello, and L. Maccone, Phys. Rev. Lett. **119**, 200502 (2017).
[16] S. Daryanoosh, S. Slussarenko, D. W. Berry, H. M. Wiseman, and G. J. Pryde, Nat. Commun. **9**, 4606 (2018).
[17] W. Górecki, R. Demkowicz-Dobrzański, H. M. Wiseman, and D. W. Berry, Phys. Rev. Lett. **124**, 030501 (2020).
[18] H. M. Wiseman, D. W. Berry, S. D. Bartlett, B. L. Higgins, and G. J. Pryde, IEEE J. Sel. Top. Quantum Electron. **15**, 1661 (2009).
[19] V. Giovannetti, S. Lloyd, and L. Maccone, Phys. Rev. Lett. **96**, 010401 (2006).
[20] D. W. Berry and H. M. Wiseman, Phys. Rev. Lett. **85**, 5098 (2000).
[21] D. W. Berry, H. M. Wiseman, and J. K. Breslin, Phys. Rev. A **63**, 053804 (2001).
[22] H. M. Wiseman, Phys. Rev. Lett. **75**, 4587 (1995).
[23] A. S. Holevo, in *Quantum Probability and Applications to the Quantum Theory of Irreversible Processes*, edited by L. Accardi, A. Frigerio, and V. Gorini (Springer, Berlin, 1984), pp. 153–172.
[24] R. Cleve, A. Ekert, C. Macchiavello, and M. Mosca, Proc. R. Soc. London A **454**, 339 (1998).
[25] R. B. Griffiths and C.-S. Niu, Phys. Rev. Lett. **76**, 3228 (1996).
[26] D. W. Berry, B. L. Higgins, S. D. Bartlett, M. W. Mitchell, G. J. Pryde, and H. M. Wiseman, Phys. Rev. A **80**, 052114 (2009).
[27] H. M. Wiseman and R. B. Killip, Phys. Rev. A **56**, 944 (1997).
[28] D. M. Greenberger, M. A. Horne, and A. Zeilinger, Phys. Today **46**, 22 (1993).
[29] T. C. Ralph and G. J. Pryde, Prog. Opt. **54**, 209 (2010).
[30] T. B. Pittman, B. C. Jacobs, and J. D. Franson, Phys. Rev. Lett. **88**, 257902 (2002).
[31] T. C. Ralph, N. K. Langford, T. B. Bell, and A. G. White, Phys. Rev. A **65**, 062324 (2002).
[32] J. L. O'Brien, G. J. Pryde, A. G. White, T. C. Ralph, and D. Branning, Nature (London) **426**, 264 (2003).
[33] N. K. Langford, T. J. Weinhold, R. Prevedel, K. J. Resch, A. Gilchrist, J. L. O'Brien, G. J. Pryde, and A. G. White, Phys. Rev. Lett. **95**, 210504 (2005).
[34] M. Kacprowicz, R. Demkowicz-Dobrzanski, W. Wasilewski, K. Banaszek, and I. A. Walmsley, Nat. Photon. **4**, 357 (2010).
[35] M. Jachura, R. Chrapkiewicz, R. Demkowicz-Dobrzanski, W. Wasilewski, and K. Banaszek, Nat. Commun. **7**, 11411 (2016).
[36] A. E. Ulanov, I. A. Fedorov, D. Sychev, P. Grangier, and A. I. Lvovsky, Nat. Commun. **7**, 11925 (2016).
[37] E. Roccia, V. Cimini, M. Sbroscia, I. Gianani, L. Ruggiero, L. Mancino, M. G. Genoni, M. A. Ricci, and M. Barbieri, Optica **5**, 1171 (2018).
[38] C. K. Hong, Z. Y. Ou, and L. Mandel, Phys. Rev. Lett. **59**, 2044 (1987).
[39] P. G. Kwiat, E. Waks, A. G. White, I. Appelbaum, and P. H. Eberhard, Phys. Rev. A **60**, R773 (1999).
[40] M. B. Agüero, A. A. Hnilo, and M. G. Kovalsky, J. Opt. Soc. Am. B **31**, 3088 (2014).
[41] A. G. White, A. Gilchrist, G. J. Pryde, J. L. O'Brien, M. J. Bremner, and N. K. Langford, J. Opt. Soc. Am. B **24**, 172 (2007).
[42] R. Jozsa, J. Mod. Opt. **41**, 2315 (1994).
[43] C. Vitelli, N. Spagnolo, L. Aparo, F. Sciarrino, E. Santamato, and L. Marrucci, Nat. Photon. **7**, 521 (2013).
[44] M. M. Weston, H. M. Chrzanowski, S. Wollmann, A. Boston, J. Ho, L. K. Shalm, V. B. Verma, M. S. Allman, S. W. Nam, R. B. Patel, S. Slussarenko, and G. J. Pryde, Opt. Express **24**, 10869 (2016).
[45] P. Senellart, G. Solomon, and A. White, Nat. Nanotechnol. **12**, 1026 (2017).
[46] S. Slussarenko and G. J. Pryde, Appl. Phys. Rev. **6**, 041303 (2019).
[47] H. J. Carmichael, *Statistical Methods in Quantum Optics 2* (Springer-Verlag, Berlin, Heidelberg, 2008).